Application of the Moment Method in the Slip and Transition Regime for Microfluidic Flows

Xiao-Jun Gu and David R. Emerson
Computational Science and Engineering Department
STFC Daresbury Laboratory
Warrington WA4 4AD
UNITED KINGDOM

xiaojun.gu@stfc.ac.uk; david.emerson@stfc.ac.uk

ABSTRACT

Gas flows in microfluidic devices suffer from non-equilibrium effects. To capture various non-equilibrium phenomena in the slip and early transition regime, the hydrodynamic system is extended from the Navier-Stokes-Fourier equations to the regularised 26 moment equations via Grad's moment method based on kinetic theory. It is shown in this lecture that the extended hydrodynamic equations can be effectively applied to micro-electro-mechanical-systems analytically and numerically. Well known non-equilibrium phenomenon, such as Knudsen layers and the Knudsen minimum, are used to validate the extended hydrodynamic model. It is demonstrated that the moment method can be used to predict gas flows in micro-electro-mechanical-systems.

1.0   INTRODUCTION

Due to the rapid development in fabrication technology for constructing micro-electro-mechanical-systems (MEMS), fluid flow at the micro- and nano-scale has received considerable attention [1]. A basic understanding of the nature of flow and heat transfer in these devices is considered essential for efficient design and control of MEMS. Engineering applications for gas microflows include miniaturised heat exchangers for cooling integrated circuits, hand-held gas chromatography systems for the detection of trace concentrations of air-borne pollutants, miniature heat pumps and novel high-throughput gas flow cytometers, etc.. Gas flows in micro-scale devices suffer from non-equilibrium effects when the gas molecular mean free path is the same order as the characteristic length of the device. The degree of non-equilibrium of a gas is generally expressed through the Knudsen number ($Kn=\lambda/L$) which is the ratio of the molecular mean free path, λ, to a typical dimension of the flow field, L. The non-equilibrium gas flow, or rarefied gas dynamics has been explored extensively for more than a century in association with high-speed high-altitude flow applications, such as space re-entry vehicles, and flows under ultra-low pressure (vacuum) conditions, where λ has a large value. Gas flow in micro-scale devices can suffer from rarefaction effects because the characteristic length of the device, L, is so small that it is comparable to the mean free path of the gas, even under atmospheric conditions. Beskok [2] compiled a typical range of gas flow regimes in terms of micro device dimension, as show in Figure 1. With the advent of MEMS, there has been a renewed impetus in the development of new and efficient approaches for modelling low-speed slip- and transitional-flows that can capture non-intuitive phenomena, such as Knudsen layers and the Knudsen minimum [3], and provide an accurate description of a gas that is not too far from thermodynamic equilibrium [4, 5].
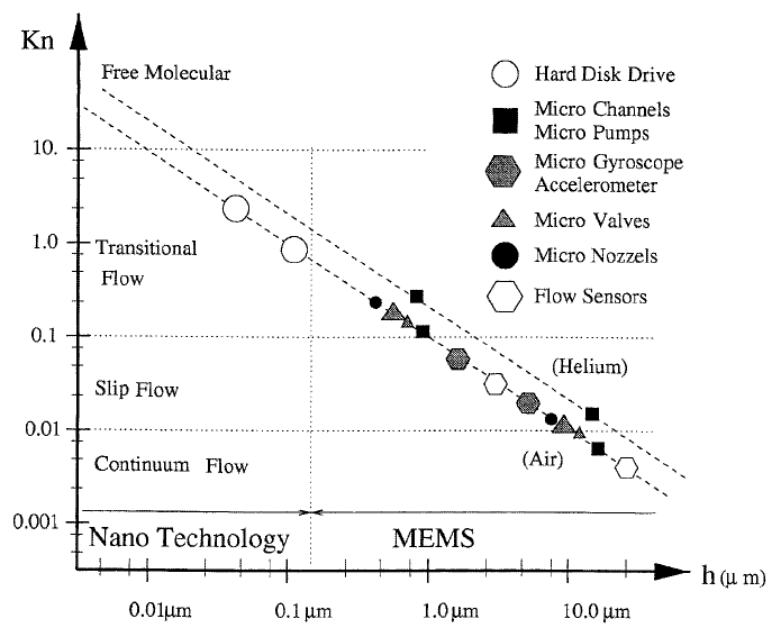
Figure 1: Characteristic length scales of typical microfluidic components and the corresponding Knudsen number at standard atmospheric conditions. Adapted from Beskok [2].

The key flow features for MEMS are that flow is laminar, typically Reynolds number $Re < 1$ and Mach number $Ma < 1$ and geometry can be complex. The different rarefaction regimes can be summarised according to the value of the Knudsen number [6]: (i) no slip ($Kn \leq 10^{-3}$); (ii) slip ($10^{-3} < Kn \leq 10^{-1}$); (iii) transition ($10^{-1} < Kn \leq 10$); and (iv) free molecular flow $Kn > 10$, respectively. Most MEMS operate at the slip and early transition regime ($Kn < 1$) as shown in figure 1. Different approaches have been employed by various researchers to capture and describe the non-equilibrium phenomena that arise due to an insufficient number of molecular collisions occurring under rarefied conditions. These approaches can be broadly divided into two specific categories: the microscopic and the macroscopic. In this lecture, the emphasis will be on the development of the macroscopic methods and their application towards engineering configurations. Microscopically, the Boltzmann equation [7] provides an accurate description of a dilute gas at all degrees of rarefaction and describes its state through a molecular distribution function that treats the gas as a large number of interacting molecules, colliding and rebounding according to prescribed laws. However, solutions of the Boltzmann equation, either directly [8, 9] or through the direct simulation Monte Carlo (DSMC) method [10], entails significant mathematical complexity and can be computationally expensive, particularly for low-speed, low Knudsen number flows in the slip and transition regime.

Due to the difficulties associated with solving the Boltzmann equation, there is significant effort being made to construct alternative solution strategies that can provide an accurate description of a gas with Knudsen numbers that extend into the transition regime. For designing components in MEMS, it is desirable that any new developments have: (i) computational efficiency comparable to conventional hydrodynamic formulations; (ii) the ability to handle real geometries, and (iii) under appropriate conditions, will recover the Navier-Stokes-Fourier solution. The two main approaches used to derive these extended hydrodynamic (EHD) equations are the Chapman-Enskog (CE) expansion [11] and the method of moments developed by Grad [12].

The Chapman-Enskog approach expands the molecular distribution function in powers of Kn to construct the constitutive relationships using the conventional hydrodynamic variables and their derivatives. The zeroth-order expansion yields the Euler equations and the first-order results in the Navier-Stokes-Fourier

(NSF) equations. In association with velocity-slip and temperature-jump wall boundary conditions, the NSF equations can predict the velocity profile in a micro-channel fairly accurately in the slip regime for isothermal flows. Higher order expansions yield the Burnett equations (second-order), Super-Burnett equations (third-order), and so on, which can be unstable in time dependent problems. In Grad's approach, a set of governing partial differential equations representing the moments of the molecular distribution function are derived from the Boltzmann equation. However, moments of higher order always appear in each moment equation and the set of moment equations is not closed. To avoid the necessity of dealing with an infinite number of moment equations, a closure procedure is required that relates the higher-order moments to those of lower order. In the seminal work of Grad [11], the set of moment equations was closed at the second-moment level, which involves 13 moments: density, momentum, energy, heat flux, and pressure deviator. It is interesting to point out that the constitutive relationships established by the Chapman-Enskog method, at any order, can be regarded as a first moment closure method with 5 moments. To close the set of moment equations at the second-moment level, Grad [11] expanded the distribution function in Hermite polynomials about the local Maxwellian to third-order accuracy and set the trace-free part of the third moments to zero. As a result, the original 13 moment equations derived by Grad (G13) are hyperbolic and lack any gradient transport mechanism. They are not suitable for computing boundary layers which appear in MEMS.

Struchtrup and Torrilhon [13] regularised Grad's 13 moment equations (R13) by applying a CE-like expansion to the governing equations of the moments higher than second order. Algebraic constitutive relationships were then established between the higher moments and the second and lower moments. The R13 equations can give reliable results for Knudsen numbers up to $Kn < 0.25$. To extend the capability of the moment method to larger Knudsen numbers in the early transition regime, we extended the regularisation theory to the 26 moment equations (R26) [14]. However, to apply the regularised moment equations to confined flows, such as those found in microfluidic channels, wall boundary conditions are required for higher moments in addition to the velocity-slip and temperature-jump conditions. We pioneered the treatment of wall boundary conditions for macroscopic variables from kinetic boundary conditions [15]. The treatment of solid boundaries was further improved by Torrilhon and Struchtrup [16]. This opens the door to solve the moment equations for flows in confined geometries.

For simple geometries, such as a straight channel or pipe, analytical solutions can be obtained from the linearised moment equations [17-21]. However, for real engineering applications of complicated geometries, numerical procedures have to be employed to obtain solutions. To numerically solve the moment equations for parabolic and elliptic flows within a conventional computational fluid dynamics (CFD) approach, such as the finite volume (FV) method, is quite challenging because the gradient transport mechanisms are not explicitly expressed in the momentum and energy equations of the moment system. The inadequacy of the standard FV method for the governing equations without any gradient transport terms is well recognised [22], so that methods for dealing with hyperbolic problems are required, such as Riemann solvers [23], TVD schemes [24] and ENO schemes [25]. These schemes are complex and computationally expensive for multidimensional confined flow, particularly at low speed. Gu and Emerson [14, 15] proposed a primitive variable transformation approach to split the higher order moments into their gradient and non-gradient transport components. Recently, a new strategy is proposed to solve the regularised moment equations on a collocated grid for low speed flows in confined geometries [26]. In this lecture, the approach to build up macroscopic governing equations by the moment method will be introduced. The procedure to solve the moment equations for low speed flows in MEMS will be described and validation examples will be given.

2.0   MOMENT METHOD

Kinetic theory accounts for a molecule's movement and interaction through a molecular phase-density distribution function, $F(\boldsymbol{\xi}, \boldsymbol{x}, t)$, which satisfies the Boltzmann integro-differential equation [6], where $\boldsymbol{x}$

and ξ are the position and velocity vectors, respectively, of a molecule at time t, and $F(\xi, x, t)dxd\xi$ gives the number of molecules whose velocities lie within $d\xi$ in a volume element dx. For convenience, a mass distribution function is used in the present study and is defined by

$$f(\xi, x, t) = mF(\xi, x, t),$$ (1)

where m is the mass of a molecule. The Boltzmann equation, expressed by [6]:

$$\frac{\partial f}{\partial t} + \xi_i \frac{\partial f}{\partial x_i} + a_i \frac{\partial f}{\partial \xi_i} = Q(f, f)$$ (2)

is the central equation in kinetic theory, the properties of which can be used to guide the development of kinetic and macroscopic models for rarefied gas flow. Here t and x_i are temporal and spatial coordinates, respectively, and any suffix i, j, k represents the usual summation convention. The external acceleration is denoted by a_i. On the right hand side of equation (2), $Q(f, f)$ is the collision integral. The most interesting feature of the Boltzmann equation is that the macroscopic irreversible process of entropy is imbedded in it, known as the *H*-theorem [6].

Kinetic theory associates hydrodynamic quantities with the moments of the distribution function. Once the distribution function, f, is known, its moments with respect to ξ can be determined. For example, the density, ρ, and the momentum, ρu_i, can be obtained from [27]:

$$\rho = \int f d\xi \quad \text{and} \quad \rho u_i = \int \xi_i f \, d\xi.$$ (3)

An intrinsic or peculiar velocity is introduced as

$$c_i = \xi_i - u_i,$$ (4)

so that the moments with respect to u_i can be conveniently calculated as

$$\rho_{i_1 i_2 \ldots i_N} = \int c_{i_1} c_{i_2} \ldots c_{i_N} f \, d\xi.$$ (5)

The pressure tensor is a second moment of the distribution function and can be separated as follows:

$$p_{ij} = \int c_i c_j f \, d\xi = p\delta_{ij} + p_{<ij>} = p\delta_{ij} + \sigma_{ij}$$ (6)

where δ_{ij} is the Kronecker delta function, $p = p_{kk}/3$ is the pressure, and $\sigma_{ij} = p_{<ij>}$ is the deviatoric stress tensor. The angular brackets denote the traceless part of a symmetric tensor. Furthermore, the thermal energy density and the heat flux vector are given, respectively, by

$$\rho\varepsilon = \frac{1}{2}\int c^2 f \, d\xi = \frac{3}{2}\rho\frac{k}{m}T = \frac{3}{2}\rho RT,$$ (7)

$$q_i = \frac{1}{2}\int c^2 c_i f \, d\xi.$$ (8)

where $c^2 = c_k c_k$. The temperature, T, is related to the pressure and density by the ideal gas law, $p = \rho(k/m)T = \rho RT$, where k is Boltzmann's constant and R is the gas constant.

Equation (2) tells us that there is only one equilibrium state and its distribution function is expressed by the Maxwellian, f_M, parameterised by traditional hydrodynamic variables, ρ, T, and u_i as [6]:

$$f_M = \frac{\rho}{\sqrt{(2\pi RT)^3}} \exp\left(-\frac{c^2}{2RT}\right). \tag{9}$$

When the gas is away from the equilibrium state, an infinite number of independent moments can be defined from equation (5). In other words, to recover the distribution function, f, at the state of non-equilibrium, an infinite number of moments are required. In the moment method, a limited number of moments are employed to approximate the non-equilibrium state.

The five collision invariants, $\boldsymbol{\psi} = (1, \xi_i, c^2)$, which satisfy [6]:

$$\int \boldsymbol{\psi}\, Q(f, f) d\boldsymbol{\xi} = 0, \tag{10}$$

lead to the conservation laws for mass, momentum and energy, respectively, as [27]:

$$\frac{\partial \rho}{\partial t} + \frac{\partial \rho u_i}{\partial x_i} = 0, \tag{11}$$

$$\frac{\partial \rho u_i}{\partial t} + \frac{\partial \rho u_i u_j}{\partial x_j} + \frac{\partial \sigma_{ij}}{\partial x_j} = -\frac{\partial p}{\partial x_i} + \rho a_i, \tag{12}$$

$$\frac{\partial \rho T}{\partial t} + \frac{\partial \rho u_i T}{\partial x_i} + \frac{2}{3R}\frac{\partial q_i}{\partial x_i} = -\frac{2}{3R}\left(p\frac{\partial u_i}{\partial x_i} + \sigma_{ij}\frac{\partial u_j}{\partial x_i}\right). \tag{13}$$

To close the above set of equations, a CE expansion of the distribution function in powers of Kn is applied to the Boltzmann equation. The traditional hydrodynamic variables, ρ, T, and u_i and their derivatives are used to estimate the values of σ_{ij} and q_i. Alternatively, the governing equations for σ_{ij}, q_i and higher moments can be derived from the Boltzmann equation. However, there appear even higher order moments in the relevant moment equations. There are various ways to close the moment equation set [28].

In the moment method proposed by Grad [11], the distribution function, f, is expanded in Hermite polynomials as:

$$f = \lim_{N\to\infty} f_M \sum_{n=0}^{N} \frac{1}{n!} a_A^{(n)} H_A^{(n)} = f_M\left(a^{(0)} H^{(0)} + a_i^{(1)} H_i^{(1)} + \frac{1}{2!} a_{ij}^{(2)} H_{ij}^{(2)} + \frac{1}{3!} a_{ijk}^{(3)} H_{ijk}^{(3)} + ...\right) \tag{14}$$

where $H_A^{(n)}$ is the Hermite function and $a_A^{(n)}$ are the coefficients. All of the polynomial coefficients are linear combinations of the moments of f. An infinite set of Hermite coefficients is equivalent to the molecular distribution function and no kinetic information is lost in such a system. In practice, the molecular distribution function has to be truncated and the specific problem to be addressed will determine the order of the truncation. Usually, the truncated distribution function is called Grad's distribution function and is denoted as f_G.

It is expected that as Kn increases, the order of the truncated Hermite polynomials should increase to provide an accurate description of the flow conditions. By choosing a sufficient number of Hermite

coefficients, a general solution of the Boltzmann equation can be approximated. The governing equations of the moments involved in the Hermite coefficients can be derived from the Boltzmann equation. However, the set of equations are not closed, since the fluxes and the collision terms are unknown. The truncated distribution function is used to calculate the collision terms and higher moments in the fluxes as functions of the chosen moments to close the equation set. All the moments included in the truncated distribution function construct the *Grad moment manifold* (GMM). These moments relax to the equilibrium state at a rate governed by their corresponding governing equations. In Grad's original approach, the remaining higher moments outside the GMM are calculated as a linear combination of the moments in the GMM without any dynamic corrections. In the regularised moment method, a CE expansion is applied to the higher order moment equations, so that the remaining higher moments outside the GMM from the truncated distribution function approach the GMM (not the equilibrium state) at a fast finite rate, then relax to the equilibrium state along with the GMM [28]. The different relaxation process models used in the construction of macroscopic equations are schematically shown in Figure 2. Circles with broken lines represent a non-equilibrium state of an infinite number of independent moments. Circles with solid line represent an equilibrium or quasi-equilibrium sate which can be represented by a finite number of independent moments. It clearly illustrates the essential role of the CE expansion in the modelling process. An infinite number of independent moments can be absorbed into a system with a finite number of moments through a CE expansion.
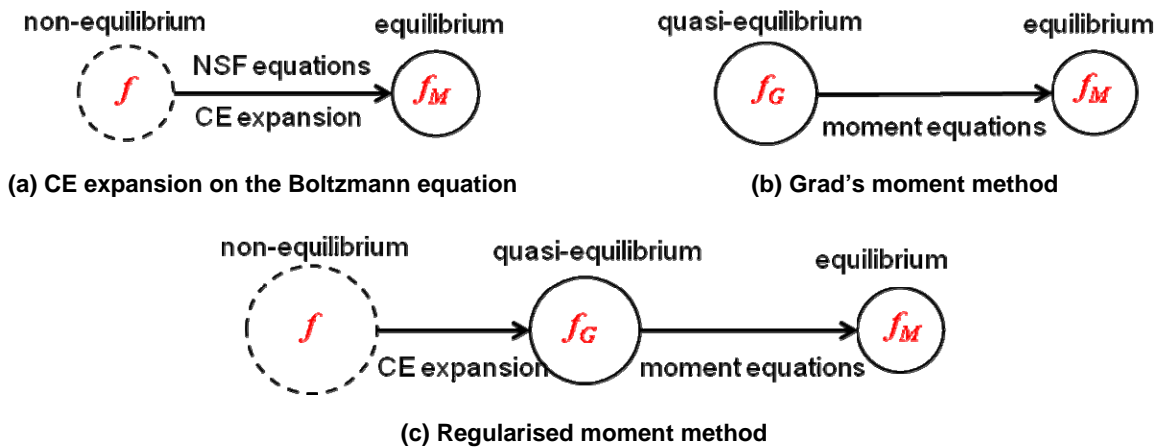

(a) CE expansion on the Boltzmann equation
(b) Grad's moment method

(c) Regularised moment method

Figure 2: Schematic modelling of relaxation process in the moment method.

2.1 Continuum Hydrodynamic Model – Navier-Stokes-Fourier Equations

The traditional hydrodynamic quantities of density, ρ, velocity, u_i, and temperature, T, correspond to the first five lowest-order moments of the molecular distribution function. The governing equations of these hydrodynamic quantities for a dilute gas can be obtained from the Boltzmann equation and represent mass, momentum, and energy conservation laws, as expressed in equations (11)-(13). The classical way to close this set of equations is through a CE expansion of the molecular distribution function in terms of Kn around the Maxwellian, which is first order in Hermite polynomials. The zeroth-order CE expansion yields the Euler equations and the first-order approximation of σ_{ij} and q_i, for Maxwell molecules, gives [10, 27]:

$$\sigma_{ij}^{NSF} = -2\mu \frac{\partial u_{<i}}{\partial x_{j>}} \text{ and } q_i^{NSF} = -\frac{15}{4} R\mu \frac{\partial T}{\partial x_i}, \tag{15}$$

in which μ is the viscosity. Equation (15) expresses an import transport mechanism for u_i and T: the gradient transport mechanism in continuum mechanics. If we let

$$\sigma_{ij} = \sigma_{ij}^{NSF} \quad \text{and} \quad q_i = q_i^{NSF} \tag{16}$$

and inserting equations (15) and (16) into equations (12) and (13) results in the traditional hydrodynamic equations, i.e. the Navier-Stokes-Fourier equations. The second order CE expansion adds the higher derivatives of the hydrodynamic variables to σ_{ij} and q_i and results in the Burnett equations.

2.2 Second Moment Closure – Regularised 13 Moment Equations

As the value of *Kn* increases, more moments need to be included in the GMM to accurately describe any non-equilibrium phenomena. Grad [11] truncated the distribution function to the incomplete third order in Hermite polynomials, f_{G13}, as:

$$f_{G13} = f_M \left\{ 1 + \frac{1}{2} \frac{\sigma_{ij}}{pRT} c_i c_j - \frac{1}{pRT} c_i q_i \left(1 - \frac{c^2}{5RT} \right) \right\}. \tag{17}$$

Grad was one of the pioneers to introduce σ_{ij} and q_i as extended hydrodynamic variables and derived a set of governing equations for them from the Boltzmann equation. For Maxwell molecules, the stress and heat flux equations are [27]:

$$\frac{\partial \sigma_{ij}}{\partial t} + \frac{\partial u_k \sigma_{ij}}{\partial x_k} + \frac{\partial m_{ijk}}{\partial x_k} = -\frac{p}{\mu} \sigma_{ij} - 2p \frac{\partial u_{<i}}{\partial x_{j>}} - \frac{4}{5} \frac{\partial q_{<i}}{\partial x_{j>}} - 2\sigma_{k<i} \frac{\partial u_{j>}}{\partial x_k}, \tag{18}$$

$$\begin{aligned} \frac{\partial q_i}{\partial t} + \frac{\partial u_j q_i}{\partial x_j} + \frac{1}{2} \frac{\partial R_{ij}}{\partial x_j} &= -\frac{2}{3} \frac{p}{\mu} q_i - \frac{5}{2} pR \frac{\partial T}{\partial x_i} - \frac{7\sigma_{ik} R}{2} \frac{\partial T}{\partial x_k} - RT \frac{\partial \sigma_{ik}}{\partial x_k} + \frac{\sigma_{ij}}{\rho} \left(\frac{\partial p}{\partial x_j} + \frac{\partial \sigma_{jk}}{\partial x_k} \right) \\ &\quad - \frac{2}{5} \left(\frac{7}{2} q_k \frac{\partial u_i}{\partial x_k} + q_k \frac{\partial u_k}{\partial x_i} + q_i \frac{\partial u_k}{\partial x_k} \right) - \frac{1}{6} \frac{\partial \Delta}{\partial x_i} - m_{ijk} \frac{\partial u_j}{\partial x_k}. \end{aligned} \tag{19}$$

If only the underlined terms in equations (18) and (19) are retained and the rest of terms are set to zero, the NSF equations are recovered. Here, m_{ijk}, R_{ij} and Δ represent the difference between the true value of the higher moments ($\rho_{<ijk>}$, $\rho_{<ij>rr}$, and ρ_{rrss}) and their approximated value with f_{G13}, respectively [13], i.e.

$$\begin{aligned} m_{ijk} &= \rho_{<ijk>} - \rho_{<ijk>|f_{G13}} = \rho_{<ijk>}, \\ R_{ij} &= \rho_{<ij>rr} - \rho_{<ij>rr|f_{G13}} = \rho_{<ij>rr} - 7RT\sigma_{ij}, \\ \Delta &= \rho_{rrss} - \rho_{rrss|f_{G13}} = \rho_{rrss} - 15pRT. \end{aligned} \tag{20}$$

In Grad's original method, such deviations were omitted, so that $m_{ijk}^{G13} = R_{ij}^{G13} = \Delta^{G13} = 0$. This results in the well known G13 equations. To close the set of equations (11)–(13), (18) and (19), Struchtrup & Torrilhon regularised the G13 equations and obtained the following closures [13, 27]:

$$m_{ijk}^{R13} = -2\frac{\mu}{p} \left(RT \frac{\partial \sigma_{<ij}}{\partial x_{k>}} + \sigma_{<ij} \frac{\partial RT}{\partial x_{k>}} - \frac{\sigma_{<ij}}{\rho} \frac{\partial p}{\partial x_{k>}} + \frac{4}{5} q_{<i} \frac{\partial u_j}{\partial x_{k>}} - \frac{\sigma_{<ij}}{\rho} \frac{\partial \sigma_{k>l}}{\partial x_l} \right), \tag{21}$$

$$R_{ij}^{R13} = -\frac{24}{5}\frac{\mu}{p}\left[RT\frac{\partial q_{<i}}{\partial x_{j>}} + 2q_{<i}\frac{\partial RT}{\partial x_{j>}} - \frac{q_{<i}}{\rho}\left(\frac{\partial p}{\partial x_{j>}} + \frac{\partial \sigma_{j>k}}{\partial x_k}\right) - \frac{5}{6}\frac{\sigma_{ij}}{\rho}\left(\frac{\partial q_k}{\partial x_k} + \sigma_{kl}\frac{\partial u_k}{\partial x_l}\right)\right.$$

$$\left. + \frac{5RT}{7}\left(\sigma_{k<i}\frac{\partial u_{j>}}{\partial x_k} + \sigma_{k<i}\frac{\partial u_k}{\partial x_{j>}} - \frac{2}{3}\sigma_{ij}\frac{\partial u_k}{\partial x_k}\right)\right] - \frac{4}{7}\frac{\sigma_{k<i}\sigma_{j>k}}{\rho}, \tag{22}$$

$$\Delta^{R13} = -12\frac{\mu}{p}\left[\frac{7}{2}q_k\frac{\partial RT}{\partial x_k} - \frac{q_j}{\rho}\left(\frac{\partial p}{\partial x_j} + \frac{\partial \sigma_{jk}}{\partial x_k}\right) + RT\left(\frac{\partial q_k}{\partial x_k} + \sigma_{ij}\frac{\partial u_i}{\partial x_j}\right)\right] - \frac{\sigma_{ij}\sigma_{ij}}{\rho}. \tag{23}$$

If we let

$$m_{ijk} = m_{ijk}^{R13}, \ R_{ij} = R_{ij}^{R13} \quad \text{and} \quad \Delta = \Delta^{R13} \tag{24}$$

and inserting equations (21)–(24) into equations (18) and (19), we obtain a set of closed 13 moment equations which is denoted as the R13 equations [13].

2.3   Higher Order Moment Closure – Regularised 26 Moment Equations

One of the challenges for macroscopic models in microflows is to capture the Knudsen layer [4]. The R13 equations improved Grad's original closure significantly, but they were not able to capture the Knudsen layer velocity profile accurately [21]. Since equations (21) and (22) are algebraic approximations for m_{ijk} and R_{ij}, they can only provide a mechanism to produce a boundary layer for the lower order moments, σ_{ij} and q_i, but have no mechanism to produce their own boundary layer near the wall. As the Knudsen layer is a linear superposition of many exponential layers in planar [29], the R13 equations only resolve one such contribution [21]. To increase the capability of the moment method, the distribution function is truncated to the incomplete fourth order in Hermite polynomials as [14]:

$$f_{G26} = f_M\left\{1 + \left[\frac{\sigma_{ij}c_ic_j}{2pRT} + \frac{c_iq_i}{pRT}\left(\frac{c^2}{5RT} - 1\right) + \frac{m_{ijk}c_ic_jc_k}{6p(RT)^2} + \frac{R_{ij}c_ic_j}{4p(RT)^2}\left(\frac{c^2}{7RT} - 1\right)\right.\right.$$

$$\left.\left. + \frac{\Delta}{8pRT}\left(\frac{c^4}{15(RT)^2} - \frac{2c^2}{3RT} + 1\right)\right]\right\}, \tag{25}$$

and the moments m_{ijk}, R_{ij} and Δ are included in the GMM as extended hydrodynamic variables. As a result, a set of 26 moment equations can be derived from the Boltzmann equation [14]:

$$\frac{\partial m_{ijk}}{\partial t} + \frac{\partial u_l m_{ijk}}{\partial x_l} + \frac{\partial \phi_{ijkl}}{\partial x_l} = -\frac{3}{2}\frac{p}{\mu}m_{ijk} - 3\left(RT\frac{\partial \sigma_{<ij}}{\partial x_{k>}} + \sigma_{<ij}\frac{\partial RT}{\partial x_{k>}} - \frac{\sigma_{<ij}}{\rho}\frac{\partial p}{\partial x_{k>}} + \frac{4}{5}q_{<i}\frac{\partial u_j}{\partial x_{k>}} - \frac{\sigma_{<ij}}{\rho}\frac{\partial \sigma_{k>l}}{\partial x_l}\right), \tag{26}$$

$$\frac{\partial R_{ij}}{\partial t} + \frac{\partial u_k R_{ij}}{\partial x_k} + \frac{\partial \psi_{ijk}}{\partial x_k} = -\frac{7}{6}\frac{p}{\mu}R_{ij} - \frac{28}{5}\left[RT\frac{\partial q_{<i}}{\partial x_{j>}} - \frac{q_{<i}}{\rho}\left(\frac{\partial p}{\partial x_{j>}} + \frac{\partial \sigma_{j>k}}{\partial x_k}\right) - \frac{5}{6}\frac{\sigma_{ij}}{\rho}\left(\frac{\partial q_k}{\partial x_k} + \sigma_{kl}\frac{\partial u_k}{\partial x_l}\right)\right.$$

$$\left. + 2q_{<i}\frac{\partial RT}{\partial x_{j>}} + \frac{5RT}{7}\left(\sigma_{k<i}\frac{\partial u_{j>}}{\partial x_k} + \sigma_{k<i}\frac{\partial u_k}{\partial x_{j>}} - \frac{2}{3}\sigma_{ij}\frac{\partial u_k}{\partial x_k}\right)\right] - \frac{2}{3}\frac{RT\sigma_{k<i}\sigma_{j>k}}{\mu}, \tag{27}$$

$$\frac{\partial \Delta}{\partial t} + \frac{\partial \Delta u_i}{\partial x_i} + \frac{\partial \Omega_i}{\partial x_i} = -\frac{2}{3}\frac{p}{\mu}\Delta - 8\left[\frac{7}{2}q_k\frac{\partial RT}{\partial x_k} - \frac{q_j}{\rho}\left(\frac{\partial p}{\partial x_j} + \frac{\partial \sigma_{jk}}{\partial x_k}\right) + RT\left(\frac{\partial q_k}{\partial x_k} + \sigma_{ij}\frac{\partial u_i}{\partial x_j}\right)\right] - \frac{2}{3}\frac{RT\sigma_{ij}\sigma_{ij}}{\mu}. \quad (28)$$

Here, ϕ_{ijkl}, ψ_{ijk} and Ω_i are the difference between the true value of the higher moments ($\rho_{<ijkl>}$, $\rho_{<ijk>rr}$, and ρ_{rrssi}) and their corresponding value approximated with f_{G26}, i.e.

$$\phi_{ijkl} = \rho_{<ijkl>} - \rho_{<ijkl>|f_{G26}} = \rho_{<ijkl>},$$
$$\psi_{ijk} = \rho_{rr<ijk>} - \rho_{rr<ijk>|f_{G26}} = \rho_{rr<ijk>} - 9RTm_{ijk}, \quad (29)$$
$$\Omega_i = \rho_{rrssi} - \rho_{rrssi|f_{G26}} = \rho_{rrssi} - 28RTq_i.$$

Following the same regularisation procedure for the 13 moment equations, the following closures for equations (26)-(28) can be readily obtained by [14]:

$$\phi_{ijkl} = -\frac{4\mu}{Z_1\rho}\left(\frac{\partial m_{<ijk}}{\partial x_{l>}} - m_{<ijk}\frac{\partial \ln \rho}{\partial x_{l>}} + \frac{3}{7RT}\left(7RT\sigma_{<ij} + R_{<ij}\right)\frac{\partial u_k}{\partial x_{l>}}\right) - \frac{Z_2}{Z_1}\frac{\sigma_{<ij}\sigma_{kl>}}{\rho}, \quad (30)$$

$$\psi_{ijk} = -\frac{27\mu}{7Y_1\rho}\left(\frac{\partial R_{<ij}}{\partial x_{k>}} - R_{<ij}\frac{\partial \ln \rho}{\partial x_{k>}} + \frac{R_{<ij} + 7RT\sigma_{<ij}}{RT}\frac{\partial RT}{\partial x_{k>}} + \frac{28}{5}q_{<i}\frac{\partial u_j}{\partial x_{k>}}\right)$$
$$-\left(\frac{Y_2}{Y_1}\frac{\sigma_{<li}m_{jkl>}}{\rho} + \frac{Y_3}{Y_1}\frac{q_{<i}\sigma_{jk>}}{\rho}\right), \quad (31)$$

$$\Omega_i = -\frac{\mu}{\rho}\left[\frac{7}{3}\frac{\partial \Delta}{\partial x_i} - \frac{7}{3}\Delta\frac{\partial \ln \rho}{\partial x_i} + 4\frac{\partial R_{ij}}{\partial x_j} - 4R_{ij}\frac{\partial \ln \rho}{\partial x_j} + \frac{56}{5}\left(q_j\frac{\partial u_i}{\partial x_j} + q_j\frac{\partial u_j}{\partial x_i}\right)\right.$$
$$\left. + 14\frac{2RT\sigma_{ij} + R_{ij}}{RT}\frac{\partial RT}{\partial x_j} + \frac{14}{3}\frac{\Delta}{RT}\frac{\partial RT}{\partial x_i}\right] - \frac{2}{15}\left(\frac{5m_{ijk}\sigma_{jk} + 14q_j\sigma_{ij}}{\rho}\right), \quad (32)$$

in which Z_1=2.097, Z_2=0.291, Y_1=1.698, Y_2=1.203 and Y_3=0.854 are collision term constants for Maxwell molecules [14, 30]. Following the convention of Struchtrup [27], the above closed set of 26 moment equations are denoted as the R26 equations. In the right hand side of the governing equations (26)–(28) for the moments m_{ijk}, R_{ij} and Δ, only the terms involved in the R13 closure are retained. Some higher order terms in the constitutive relationships (30)–(32), which have negligible effects for flows in MEMS, are neglected. The full list of equations and their closures can be found in Ref. [14].

4.0   WALL BOUNDARY CONDITIONS

To apply any of the foregoing models to flows in confined geometries, appropriate wall boundary conditions are required to determine a unique solution. One of the difficulties encountered in any investigation of wall boundary conditions is due to a limited understanding of the structure of surface layers of solid bodies and of the effective interaction potential of the gas molecules with the wall. A scattering kernel represents a fundamental concept in gas-surface interactions, by means of which other quantities should be defined [2]. For the moment equations, the boundary conditions for the relevant macroscopic variables are required in addition to the traditional velocity slip and temperature jump conditions. As we can derive the macroscopic governing equations from kinetic theory, the macroscopic boundary conditions can also be constructed from kinetic theory. Gu & Emerson [14, 15] obtained a set of

wall boundary conditions for the R13 moment equations based on Maxwell's kinetic wall boundary model [31] and a fourth-order approximation of the molecular distribution function in Hermite polynomials. To construct wall boundary conditions for the R26 equations, a fifth order approximation of the molecular distribution function, $f^{(5)}$, is required, which can be expressed as [14]:

$$f^{(5)} = f_{G26} + f_M \left[\frac{\phi_{ijkl} c_i c_j c_k c_l}{24 p (RT)^3} + \frac{\psi_{ijk} c_i c_j c_k}{12 p (RT)^3} \left(\frac{c^2}{9RT} - 1 \right) + \frac{c_i \Omega_i}{40 p (RT)^2} \left(\frac{c^4}{7(RT)^2} - \frac{2c^2}{RT} + 5 \right) \right]. \qquad (33)$$

It should be noted that the higher moments involved in the underlined terms in equation (33) arise from the regularisation procedure.

Maxwell's kinetic boundary condition [31] is one of the simplest models and it states that a fraction, α, will be *diffusely* reflected with a Maxwellian distribution, f_M^w, at the temperature of the wall, T_w, while the remaining fraction (1-α), of gas molecules will undergo *specular* reflection. In a frame where the coordinates are attached to the wall, with n_i the normal vector of the wall pointing towards the gas and τ_i the tangential vector of the wall, such that all molecules with $\xi_i n_i < 0$ are incident upon the wall and molecules with $\xi_i n_i \geq 0$ are emitted by the wall, Maxwell's boundary condition can be expressed by [27]:

$$f^w = \begin{cases} \alpha f_M^w + (1-\alpha) f(-\xi_i n_i), & \xi_i n_i \geq 0, \\ f(\xi_i n_i), & \xi_i n_i < 0. \end{cases} \qquad (34)$$

By definition, the value of any moment at the wall can be obtained from

$$\int_{\xi_i n_i \geq 0} c_{i_1} c_{i_2} \cdots c_{i_n} f(\xi_i n_i) d\boldsymbol{\xi} = \int_{\xi_i n_i \geq 0} c_{i_1} c_{i_2} \cdots c_{i_n} \left[\alpha f_M^w + (1-\alpha) f(-\xi_i n_i) \right] d\boldsymbol{\xi}. \qquad (35)$$

From the analysis of the special case of $\alpha = 0$, it was found that only moments that are odd functions of $c_i n_i$ can be used to construct wall boundary conditions [11]. Furthermore, only those moments representing fluxes can be used in the boundary conditions [16]. From equation (35), the slip velocity parallel to the wall, u_τ, and temperature jump conditions can be obtained as [14, 15]:

$$u_\tau = -\frac{2-\alpha}{\alpha} \sqrt{\frac{\pi RT}{2}} \frac{\sigma_{n\tau}}{p_\alpha} - \frac{5m_{nn\tau} + 2q_\tau}{10 p_\alpha} + \frac{9\Omega_\tau + 70\psi_{nn\tau}}{2520 p_\alpha RT}, \qquad (36)$$

$$RT - RT_w = -\frac{2-\alpha}{\alpha} \sqrt{\frac{\pi RT}{2}} \frac{q_n}{2 p_\alpha} - \frac{RT\sigma_{nn}}{4 p_\alpha} + \frac{u_\tau^2}{4} - \frac{75R_{nn} + 28\Delta}{840 p_\alpha} + \frac{\phi_{nnnn}}{24 p_\alpha} \qquad (37)$$

where

$$p_\alpha = p + \frac{\sigma_{nn}}{2} - \frac{30R_{nn} + 7\Delta}{840 RT} - \frac{\phi_{nnnn}}{24 RT}. \qquad (38)$$

Here $\sigma_{nn} = \sigma_{ij} n_i n_j$, $\sigma_{n\tau} = \sigma_{ij} n_i \tau_j$, $q_\tau = q_i \tau_i$, $q_n = q_i n_i$, $m_{nn\tau} = m_{ijk} n_i n_j \tau_k$, $m_{nnn} = m_{ijk} n_i n_j n_k$, $R_{nn} = R_{ij} n_i n_j$, $\Omega_\tau = \Omega_i \tau_i$, $\psi_{nn\tau} = \psi_{ijk} n_i n_j \tau_k$, and $\phi_{nnnn} = \phi_{ijkl} n_i n_j n_k n_l$ are the tangential and normal components of σ_{ij}, q_i, m_{ijk}, R_{ij}, ψ_{ijk}, Ω_i and ϕ_{ijkl} relative to the wall, respectively. It should be noted that the normal velocity at the wall, $u_n = 0$, since there is no gas flow through the wall. Equations (36) and (37) are similar to the slip velocity and temperature jump conditions for the NSF equations [5, 6] with the underlined terms on the right hand side

providing higher-order moment corrections. These underlined terms can be related to second- or higher-order velocity slip and temperature jump boundary conditions. The slip velocity in the higher moment system is not only proportional to the shear stress, $\sigma_{n\tau}$, but also to the tangential heat flux, q_τ, and other higher moments. With a normalised slip velocity, $\hat{u}_\tau = u_\tau / \sqrt{RT}$, and a normalised wall temperature, $\hat{T}_w = T_w / T$, the rest of the wall boundary conditions are [14]:

$$\sigma_{\tau\tau} = -\frac{2-\alpha}{\alpha}\sqrt{\frac{\pi RT}{2}}\left(\frac{5m_{n\tau\tau}+2q_n}{5RT}\right) + p_\alpha\left(\hat{u}_\tau^2 + \hat{T}_w - 1\right) - \frac{R_{\tau\tau}+R_{nn}}{14RT} - \frac{\Delta}{30RT} - \frac{\phi_{nn\tau\tau}}{2RT}, \tag{39}$$

$$\sigma_{nn} = -\frac{2-\alpha}{\alpha}\sqrt{\frac{\pi RT}{2}}\left(\frac{5m_{nnn}+6q_n}{10RT}\right) + p_\alpha\left(\hat{T}_w - 1\right) - \frac{R_{nn}}{7RT} - \frac{\Delta}{30RT} - \frac{\phi_{nnnn}}{6RT}, \tag{40}$$

$$q_\tau = -\frac{5}{18}\frac{2-\alpha}{\alpha}\sqrt{\frac{\pi RT}{2}}\left(7\sigma_{n\tau} + \frac{R_{n\tau}}{RT}\right) - \frac{5\hat{u}_\tau p_\alpha \sqrt{RT}\left(\hat{u}_\tau^2 + 6\hat{T}_w\right)}{18} - \frac{10m_{nn\tau}}{9} - \frac{5\psi_{nn\tau}}{81RT} - \frac{\Omega_\tau}{56RT}, \tag{41}$$

$$m_{\tau\tau\tau} = -\frac{2-\alpha}{\alpha}\sqrt{\frac{\pi RT}{2}}\left(3\sigma_{n\tau} + \frac{3R_{n\tau}}{7RT} + \frac{\phi_{n\tau\tau\tau}}{RT}\right) - p_\alpha\hat{u}_\tau\sqrt{RT}\left(\hat{u}_\tau^2 + 3\hat{T}_w\right) - \frac{3m_{nn\tau}}{2} - \frac{9q_\tau}{5} - \frac{9\Omega_\tau}{280RT}$$
$$- \frac{2\psi_{\tau\tau\tau}+3\psi_{nn\tau}}{36RT}, \tag{42}$$

$$m_{nn\tau} = -\frac{2-\alpha}{\alpha}\sqrt{\frac{\pi RT}{2}}\left(\sigma_{\tau n} + \frac{R_{n\tau}}{7RT} + \frac{\phi_{nnn\tau}}{3RT}\right) - \frac{2}{5}q_\tau - \frac{2\hat{T}_w\hat{u}_\tau p_\alpha\sqrt{RT}}{3} - \frac{\psi_{nn\tau}}{18RT} - \frac{\Omega_\tau}{140RT}, \tag{43}$$

$$R_{\tau\tau} = -\frac{2-\alpha}{\alpha}\sqrt{\frac{\pi RT}{2}}\left(\frac{28q_n}{15} + \frac{14m_{n\tau\tau}}{3} + \frac{\Omega_n}{15RT} + \frac{14\psi_{n\tau\tau}}{27RT}\right) + \frac{7p_\alpha RT\left(\hat{u}_\tau^4 + 6\hat{T}_w\hat{u}_\tau^2 + 3\hat{T}_w^2 - 3\right)}{9}$$
$$- \frac{14RT\sigma_{\tau\tau}}{3} - \frac{R_{nn}}{3} - \frac{14\Delta}{45} - \frac{7\left(\phi_{\tau\tau\tau\tau}+3\phi_{nn\tau\tau}\right)}{9}, \tag{44}$$

$$R_{nn} = -\frac{2-\alpha}{\alpha}\sqrt{\frac{\pi RT}{2}}\left(\frac{21q_n}{8} + \frac{35m_{nnn}}{16} + \frac{35\psi_{nnn}}{144RT} + \frac{3\Omega_n}{32RT}\right) + \frac{7p_\alpha RT\left(\hat{T}_w^2 - 1\right)}{4} - \frac{7RT\sigma_{nn}}{2}$$
$$- \frac{7\Delta}{30} - \frac{7\phi_{nnnn}}{6}, \tag{45}$$

$$\Delta = -\frac{35}{4}\frac{2-\alpha}{\alpha}\sqrt{\frac{\pi RT}{2}}\left(q_n + \frac{\Omega_n}{28RT}\right) - \frac{5}{4}p_\alpha RT\left(6 - 6\hat{T}_w^2 - \frac{\hat{u}_\tau^4}{4} - 3\hat{u}_\tau^2\hat{T}_w\right) - \frac{15}{4}RT\sigma_{nn}$$
$$- \frac{15}{8}R_{nn} + \frac{35}{48}\phi_{nnnn}. \tag{46}$$

5.0   LINEARISATION OF MOMENT EQUATIONS

One of the main features for gas flow in MEMS is low Reynolds number, $Re < 1$ and low Mach number $Ma < 1$. In most cases, it is sufficient to apply a linearised moment equation set to flow in the micro-system. For flows with small deviations from an equilibrium state given by ρ_o, T_o, (or, p_o) and $u_{i,o}$, these

deviations can be represented by dimensionless variables $\bar{\rho}$, $\bar{T}$, $\bar{u}_i$, $\bar{\sigma}_{ij}$, $\bar{q}_i$, $\bar{m}_{ijk}$, $\bar{R}_{ij}$, $\bar{\Delta}$, $\bar{\phi}_{ijkl}$, $\bar{\psi}_{ijk}$ and $\bar{\Omega}_i$ in

$$\rho = \rho_o\left(1+\bar{\rho}\right), \qquad T = T_o\left(1+\bar{T}\right), \qquad p = p_o\left(1+\bar{p}\right), \qquad u_i = \sqrt{RT_o}\,\bar{u}_i,$$

$$\sigma_{ij} = \rho_o RT_o \bar{\sigma}_{ij}, \quad q_i = \rho_o\left(RT_o\right)^{3/2}\bar{q}_i, \quad m_{ijk} = \rho_o\left(RT_o\right)^{3/2}\bar{m}_{ijk}, \quad R_{ij} = \rho_o\left(RT_o\right)^2 \bar{R}_{ij},$$

$$\Delta = \rho_o\left(RT_o\right)^2 \bar{\Delta}, \quad \phi_{ijkl} = \rho_o\left(RT_o\right)^2 \bar{\phi}_{ijkl}, \quad \psi_{ijk} = \rho_o\left(RT_o\right)^{5/2}\bar{\psi}_{ijk}, \quad \Omega_i = \rho_o\left(RT_o\right)^{5/2}\bar{\Omega}_i,$$

$$x_i = L\bar{x}_i, \qquad t = \left(L/\sqrt{RT_o}\right)\bar{t}, \tag{47}$$

in which, L is a characteristic length of the microsystem. Inserting equations (47) into equations (11) to (13), (18)-(19) and (26)-(28) and keeping only the terms that are linear in the deviations, a set of linearised R26 moment equations (LR26) are obtained as [19]:

$$\frac{\partial\bar{\rho}}{\partial\bar{t}} + \frac{\partial\bar{u}_i}{\partial\bar{x}_i} = 0, \tag{48}$$

$$\frac{\partial\bar{u}_i}{\partial\bar{t}} + \frac{\partial\bar{\sigma}_{ij}}{\partial\bar{x}_j} = -\frac{\partial\bar{p}}{\partial\bar{x}_i} + \frac{La_i}{RT_o}, \tag{49}$$

$$\frac{\partial\bar{p}}{\partial\bar{t}} + \frac{2}{3}\frac{\partial\bar{q}_i}{\partial\bar{x}_i} = -\frac{5}{3}\frac{\partial\bar{u}_i}{\partial\bar{x}_i}, \tag{50}$$

$$\frac{\partial\bar{\sigma}_{ij}}{\partial\bar{t}} + \frac{\partial\bar{m}_{ijk}}{\partial\bar{x}_k} = -\sqrt{\frac{\pi}{2}}\frac{L}{\lambda}\bar{\sigma}_{ij} - 2\frac{\partial\bar{u}_{<i}}{\partial\bar{x}_{j>}} - \frac{4}{5}\frac{\partial\bar{q}_{<i}}{\partial\bar{x}_{j>}}, \tag{51}$$

$$\frac{\partial\bar{q}_i}{\partial\bar{t}} + \frac{1}{2}\frac{\partial\bar{R}_{ij}}{\partial\bar{x}_j} = -\frac{2}{3}\sqrt{\frac{\pi}{2}}\frac{L}{\lambda}\bar{q}_i - \frac{5}{2}\frac{\partial\bar{T}}{\partial\bar{x}_i} - \frac{\partial\bar{\sigma}_{ik}}{\partial\bar{x}_k} - \frac{1}{6}\frac{\partial\bar{\Delta}}{\partial\bar{x}_i}, \tag{52}$$

$$\frac{\partial\bar{m}_{ijk}}{\partial\bar{t}} + \frac{\partial\bar{\phi}_{ijkl}}{\partial\bar{x}_l} = -\frac{3}{2}\sqrt{\frac{\pi}{2}}\frac{L}{\lambda}\bar{m}_{ijk} - 3\frac{\partial\bar{\sigma}_{<ij}}{\partial\bar{x}_{k>}}, \tag{53}$$

$$\frac{\partial\bar{R}_{ij}}{\partial\bar{t}} + \frac{\partial\bar{\psi}_{ijk}}{\partial\bar{x}_k} = -\frac{7}{6}\sqrt{\frac{\pi}{2}}\frac{L}{\lambda}\bar{R}_{ij} - \frac{28}{5}\frac{\partial\bar{q}_{<i}}{\partial\bar{x}_{j>}}, \tag{54}$$

$$\frac{\partial\bar{\Delta}}{\partial\bar{t}} + \frac{\partial\bar{\Omega}_i}{\partial\bar{x}_i} = -\frac{2}{3}\sqrt{\frac{\pi}{2}}\frac{L}{\lambda}\bar{\Delta} - 8\frac{\partial\bar{q}_i}{\partial\bar{x}_i}. \tag{55}$$

The linearised constitutive relationships are:

$$\bar{\phi}_{ijkl} = -\frac{4}{Z_1}\sqrt{\frac{2}{\pi}}\frac{\lambda}{L}\frac{\partial\bar{m}_{<ijk}}{\partial\bar{x}_{l>}}, \tag{56}$$

$$\overline{\psi}_{ijk} = -\frac{27}{7Y_1}\sqrt{\frac{2}{\pi}}\frac{\lambda}{L}\frac{\partial \overline{R}_{<ij}}{\partial \overline{x}_{k>}}, \tag{57}$$

$$\overline{\Omega}_i = -\frac{7}{3}\sqrt{\frac{2}{\pi}}\frac{\lambda}{L}\frac{\partial \overline{\Delta}}{\partial \overline{x}_i} - 4\sqrt{\frac{2}{\pi}}\frac{\lambda}{L}\frac{\partial \overline{R}_{ij}}{\partial \overline{x}_j} \tag{58}$$

along with the linearised boundary conditions:

$$\overline{u}_\tau = -\frac{2-\alpha}{\alpha}\sqrt{\frac{\pi}{2}}\overline{\sigma}_{n\tau} - \frac{5\overline{m}_{nn\tau}+2\overline{q}_\tau}{10} + \frac{9\overline{\Omega}_\tau + 70\overline{\psi}_{nn\tau}}{2520}, \tag{59}$$

$$\overline{T} = -\frac{2-\alpha}{\alpha}\sqrt{\frac{\pi}{2}}\frac{\overline{q}_n}{2} - \frac{\overline{\sigma}_{nn}}{4} - \frac{75\overline{R}_{nn}+28\overline{\Delta}}{840} + \frac{\overline{\phi}_{nnnn}}{24} + \frac{T_w}{T_o} - 1, \tag{60}$$

$$\overline{\sigma}_{\tau\tau} = -\frac{2-\alpha}{\alpha}\sqrt{\frac{\pi}{2}}\left(\frac{5\overline{m}_{n\tau\tau}+2q_n}{5}\right) - \frac{\overline{R}_{\tau\tau}+\overline{R}_{nn}}{14} - \frac{\overline{\Delta}}{30} - \frac{\overline{\phi}_{nn\tau\tau}}{2}, \tag{61}$$

$$\overline{\sigma}_{nn} = -\frac{2-\alpha}{\alpha}\sqrt{\frac{\pi}{2}}\left(\frac{5\overline{m}_{nnn}+6\overline{q}_n}{10}\right) - \frac{\overline{R}_{nn}}{7} - \frac{\overline{\Delta}}{30} - \frac{\overline{\phi}_{nnnn}}{6}, \tag{62}$$

$$\overline{q}_\tau = -\frac{5}{18}\frac{2-\alpha}{\alpha}\sqrt{\frac{\pi}{2}}\left(7\overline{\sigma}_{n\tau}+\overline{R}_{n\tau}\right) - \frac{5\overline{u}_\tau}{3} - \frac{10\overline{m}_{nn\tau}}{9} - \frac{5\overline{\psi}_{nn\tau}}{81} - \frac{\overline{\Omega}_\tau}{56}, \tag{63}$$

$$\overline{m}_{\tau\tau\tau} = -\frac{2-\alpha}{\alpha}\sqrt{\frac{\pi}{2}}\left(3\overline{\sigma}_{n\tau}+\frac{3\overline{R}_{n\tau}}{7}+\overline{\phi}_{n\tau\tau\tau}\right) - 3\overline{u}_\tau - \frac{3\overline{m}_{nn\tau}}{2} - \frac{9\overline{q}_\tau}{5} - \frac{9\overline{\Omega}_\tau}{280} - \frac{2\overline{\psi}_{\tau\tau\tau}+3\overline{\psi}_{nn\tau}}{36}, \tag{64}$$

$$\overline{m}_{nn\tau} = -\frac{2-\alpha}{\alpha}\sqrt{\frac{\pi}{2}}\left(\overline{\sigma}_{\tau n}+\frac{\overline{R}_{n\tau}}{7}+\frac{\overline{\phi}_{nnn\tau}}{3}\right) - \frac{2}{5}\overline{q}_\tau - \frac{2\overline{u}_\tau}{3} - \frac{\overline{\psi}_{nn\tau}}{18} - \frac{\overline{\Omega}_\tau}{140}, \tag{65}$$

$$\overline{R}_{\tau\tau} = -\frac{2-\alpha}{\alpha}\sqrt{\frac{\pi}{2}}\left(\frac{28\overline{q}_n}{15}+\frac{14\overline{m}_{nn\tau}}{3}+\frac{\overline{\Omega}_n}{15}+\frac{14\overline{\psi}_{n\tau\tau}}{27}\right) - \frac{14\overline{\sigma}_{\tau\tau}}{3} - \frac{\overline{R}_{nn}}{3} - \frac{14\overline{\Delta}}{45} - \frac{7\left(\overline{\phi}_{\tau\tau\tau\tau}+3\overline{\phi}_{nn\tau\tau}\right)}{9}, \tag{66}$$

$$\overline{R}_{nn} = -\frac{2-\alpha}{\alpha}\sqrt{\frac{\pi}{2}}\left(\frac{21\overline{q}_n}{8}+\frac{35\overline{m}_{nnn}}{16}+\frac{35\overline{\psi}_{nnn}}{144}+\frac{3\overline{\Omega}_n}{32}\right) - \frac{7\overline{\sigma}_{nn}}{2} - \frac{7\overline{\Delta}}{30} - \frac{7\overline{\phi}_{nnnn}}{6}, \tag{67}$$

$$\overline{\Delta} = -\frac{35}{4}\frac{2-\alpha}{\alpha}\sqrt{\frac{\pi}{2}}\left(\overline{q}_n+\frac{\overline{\Omega}_n}{28}\right) - \frac{15}{4}\overline{\sigma}_{nn} - \frac{15}{8}\overline{R}_{nn} + \frac{35}{48}\overline{\phi}_{nnnn}, \tag{68}$$

in which,

$$\lambda = \frac{\mu}{p_o}\sqrt{\frac{\pi R T_o}{2}} \tag{69}$$

is the mean free path. For flows in simply geometries, such as Couette and Poiseuille flows, the above linearised moment equations can be decoupled into three sets of equations related to (i) velocity, (ii)

temperature and (iii) the remaining equations. For example, for the one dimensional planar configuration, the coordinates are chosen such that the wall is parallel to the x direction and y is the direction perpendicular to the wall. The velocity in the x direction is u and the velocity in the other directions is zero. All derivatives in the x direction, except pressure gradient in Poiseuille flow, are zero everywhere and mass conservation is satisfied automatically. The equations involved in the velocity problem from the linearised R26 moment system (LR26) reduce to the following five moment system:

$$\frac{\partial \bar{u}}{\partial \bar{t}} + \frac{\partial \bar{\sigma}_{xy}}{\partial \bar{y}} = -\frac{\partial \bar{p}}{\partial \bar{x}}, \tag{70}$$

$$\frac{\partial \bar{\sigma}_{xy}}{\partial \bar{t}} + \frac{\partial \bar{m}_{xyy}}{\partial \bar{y}} = -\sqrt{\frac{\pi}{2}}\frac{L}{\lambda}\bar{\sigma}_{xy} - \frac{\partial}{\partial \bar{y}}\left(\bar{u} + \frac{2}{5}\bar{q}_x\right), \tag{71}$$

$$\frac{\partial \bar{q}_x}{\partial \bar{t}} + \frac{1}{2}\frac{\partial \bar{R}_{xy}}{\partial \bar{y}} = -\frac{2}{3}\sqrt{\frac{\pi}{2}}\frac{L}{\lambda}\bar{q}_x - \frac{\partial \bar{\sigma}_{xy}}{\partial \bar{y}}, \tag{72}$$

$$\frac{\partial \bar{m}_{xyy}}{\partial \bar{t}} + \frac{\partial \bar{\phi}_{xyyy}}{\partial \bar{y}} = -\frac{3}{2}\sqrt{\frac{\pi}{2}}\frac{L}{\lambda}\bar{m}_{xyy} - \frac{8}{5}\frac{\partial \bar{\sigma}_{xy}}{\partial \bar{y}}, \tag{73}$$

$$\frac{\partial \bar{R}_{xy}}{\partial \bar{t}} + \frac{\partial \bar{\psi}_{xyy}}{\partial \bar{y}} = -\frac{7}{6}\sqrt{\frac{\pi}{2}}\frac{L}{\lambda}\bar{R}_{xy} - \frac{14}{5}\frac{\partial \bar{q}_x}{\partial \bar{y}} \tag{74}$$

with the associated wall boundary conditions (59), (63) and (65), and the following constitutive relationships:

$$\bar{\phi}_{xyyy} = -\frac{15}{7Z_1}\sqrt{\frac{2}{\pi}}\frac{\lambda}{L}\frac{\partial \bar{m}_{xyy}}{\partial \bar{y}}, \quad \bar{\psi}_{xyy} = -\frac{72}{35Y_1}\sqrt{\frac{2}{\pi}}\frac{\lambda}{L}\frac{\partial \bar{R}_{xy}}{\partial \bar{y}} \quad \text{and} \quad \bar{\Omega}_x = -4\sqrt{\frac{2}{\pi}}\frac{\lambda}{L}\frac{\partial \bar{R}_{xy}}{\partial \bar{y}}. \tag{75}$$

6.0   NUMERICAL SOLUTION OF THE MOMENT EQUATIONS

The moment method results in a set of partial differential governing equations of mixed first and second order. In most situations, there are no analytical solutions for this complex set of governing equations and a numerical procedure is therefore required. However, in the moment equation system, the momentum and energy conservation equations are the first order partial differential equations, in which there is no explicit gradient transport mechanism. The inadequacy of the standard finite volume method for the governing equations without any gradient transport terms is well recognised [22], so that methods for dealing with hyperbolic problems are required. In the case of low-speed rarefied gas flow, such as those found in micro-devices, the flow is parabolic or elliptic. Using a hyperbolic flow solver to solve elliptic flows is inefficient and expensive. In fact, the gradient transport mechanism of the low moments is embedded in the moments one order higher. For example, the diffusion of u_i is included in σ_{ij}, and the diffusion of T is included in q_i, as reflected by the underline terms on the right hand of equations (18) and (19). To restore the gradient transport mechanism back to the moment equation system, a primitive variable transformation was introduced by decomposing the moments into their gradient and non-gradient components. The resultant equations of the non-gradient components have the general convection–diffusion form [14, 15]. Alternatively, the gradient transport mechanism can be introduced into the discretised moment equations in a collocated grid by a properly constructing the flux in the control volume face [26].

For a two dimensional steady state flow, the momentum equation (12) can be written in Cartesian coordinates (x, y) as

$$\frac{\partial \rho UU}{\partial x} + \frac{\partial \rho VU}{\partial y} + \frac{\partial \sigma_{xx}}{\partial x} + \frac{\partial \sigma_{xy}}{\partial y} = -\frac{\partial p}{\partial x},$$ (76)

$$\frac{\partial \rho UV}{\partial x} + \frac{\partial \rho VV}{\partial y} + \frac{\partial \sigma_{xy}}{\partial x} + \frac{\partial \sigma_{yy}}{\partial y} = -\frac{\partial p}{\partial y},$$ (77)

in which, U and V are the gas velocity in x and y direction, respectively. In a collocated grid arrangement shown in Figure 3, all the variables are stored at the control volume centre P and its neighboring points $WW\ W\ P\ E\ EE\ SS\ S\ N\ NN$. A discrete approximation to equation (76) or (77), in which U or V is the primitive variable, is achieved by integrating the equation over a macro-control volume surrounding the nodal point P,

$$\int_s^n \int_w^e \left(\frac{\partial \rho UU}{\partial x} + \frac{\partial \sigma_{xx}}{\partial x} \right) dxdy + \int_s^n \int_w^e \left(\frac{\partial \rho VU}{\partial y} + \frac{\partial \sigma_{xy}}{\partial y} \right) dxdy = \int_s^n \int_w^e \left(-\frac{\partial p}{\partial x} \right) dxdy$$ (78)

where n, s, e and w refer to the location of the space average of any quantity prevailing over the faces of the control volume. Using the mean-value theorem, equation (78) can be written as:

$$\left[\frac{(\rho UU)_e - (\rho UU)_w}{\delta x} + \frac{(\sigma_{xx})_e - (\sigma_{xx})_w}{\delta x} \right] \delta x \delta y + \left[\frac{(\rho VU)_n - (\rho VU)_s}{\delta y} + \frac{(\sigma_{xy})_n - (\sigma_{xy})_s}{\delta y} \right] \delta x \delta y$$

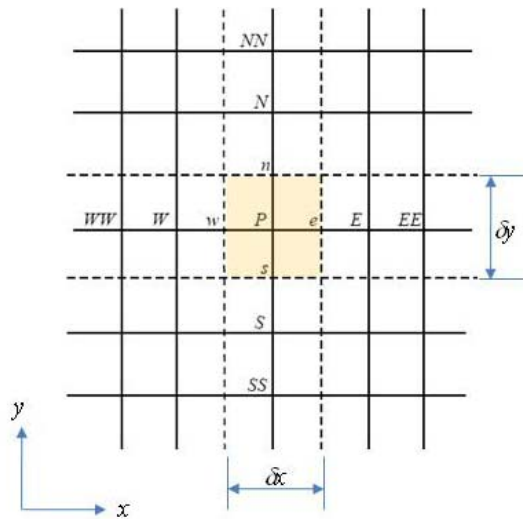$$= \left(-\frac{\delta p}{\delta x} \right)_P \delta x \delta y.$$ (79)

Figure 3: Collocated grid arrangement.

As suggested by the underline terms in the right hand side of equation (18), the stress in the momentum equation is proportional to the velocity gradient. In the discretised form in x direction, the normal stress on the nodal points, P, W and E should have

$$\left(\sigma_{xx}\right)_P \propto -\left(\mu\frac{\delta U}{\delta x}\right)_P, \quad \left(\sigma_{xx}\right)_W \propto -\left(\mu\frac{\delta U}{\delta x}\right)_W \quad \text{and} \quad \left(\sigma_{xx}\right)_E \propto -\left(\mu\frac{\delta U}{\delta x}\right)_E. \tag{80}$$

The stress at the control volume faces, *w* and *e* should have the same property as:

$$\left(\sigma_{xx}\right)_w \propto -\left(\mu\frac{\delta U}{\delta x}\right)_w \quad \text{and} \quad \left(\sigma_{xx}\right)_e \propto -\left(\mu\frac{\delta U}{\delta x}\right)_e. \tag{81}$$

To estimate the values of the stresses at the faces of the control volume, it is important to preserve this property. To guarantee this, it is convenient to interpolate the face value of the normal stress as:

$$\begin{cases} \left(\sigma_{xx}\right)_w = \frac{1}{2}\left[\left(\sigma_{xx}\right)_W + \left(\sigma_{xx}\right)_P\right] + \frac{1}{2}\left[\left(\mu\frac{\delta U}{\delta x}\right)_W + \left(\mu\frac{\delta U}{\delta x}\right)_P\right] - \left(\mu\frac{\delta U}{\delta x}\right)_w, \\[3mm] \left(\sigma_{xx}\right)_e = \frac{1}{2}\left[\left(\sigma_{xx}\right)_E + \left(\sigma_{xx}\right)_P\right] + \frac{1}{2}\left[\left(\mu\frac{\delta U}{\delta x}\right)_E + \left(\mu\frac{\delta U}{\delta x}\right)_P\right] - \left(\mu\frac{\delta U}{\delta x}\right)_e. \end{cases} \tag{82}$$

Similar interpolation of the face value of the shear stress in the *y* direction can be obtained as

$$\begin{cases} \left(\sigma_{xy}\right)_s = \frac{1}{2}\left[\left(\sigma_{xy}\right)_S + \left(\sigma_{xy}\right)_P\right] + \frac{1}{2}\left[\left(\mu\frac{\delta U}{\delta y}\right)_S + \left(\mu\frac{\delta U}{\delta y}\right)_P\right] - \left(\mu\frac{\delta U}{\delta y}\right)_s, \\[3mm] \left(\sigma_{xy}\right)_n = \frac{1}{2}\left[\left(\sigma_{xy}\right)_N + \left(\sigma_{xy}\right)_P\right] + \frac{1}{2}\left[\left(\mu\frac{\delta U}{\delta y}\right)_N + \left(\mu\frac{\delta U}{\delta y}\right)_P\right] - \left(\mu\frac{\delta U}{\delta y}\right)_n. \end{cases} \tag{83}$$

Inserting equations (82) and (83) into equation (79), the discritised momentum equation in the *x* direction can be expressed by

$$\begin{aligned} &\frac{\delta(\rho UU)}{\delta x} + \frac{\delta(\rho VU)}{\delta y} - \frac{\delta}{\delta x}\left(\mu\frac{\delta U}{\delta x}\right) - \frac{\delta}{\delta y}\left(\mu\frac{\delta U}{\delta y}\right) \\[2mm] &= \left(-\frac{\delta p}{\delta x}\right)_P - \frac{1}{2\delta x}\left\{\left[\left(\sigma_{xx}\right)_E + \left(\mu\frac{\delta U}{\delta x}\right)_E\right] - \left[\left(\sigma_{xx}\right)_W + \left(\mu\frac{\delta U}{\delta x}\right)_W\right]\right\} \\[2mm] &\quad - \frac{1}{2\delta y}\left\{\left[\left(\sigma_{xy}\right)_N + \left(\mu\frac{\delta U}{\delta y}\right)_N\right] - \left[\left(\sigma_{xy}\right)_S + \left(\mu\frac{\delta U}{\delta y}\right)_S\right]\right\}. \end{aligned} \tag{84}$$

Equation (84) is a typical discritised convective and diffusion equation with source terms on the right hand side. The same procedure can be performed to equations (77), (13), (18) and (19). Numerical methods for solving the convective and diffusion equations are well documented for both high and low speed flows [22]. For the convective terms, a range of upwind schemes including QUICK [32], SMART [33], and CUBISTA [34] are available in the literature. The diffusive and source terms are discretised by a central difference scheme and the CUBISTA scheme was selected for the present study. The coupling of the velocity and pressure fields is through the SIMPLE [35] or PISO [36] algorithm. For steady state flow, the system of equations can be solved iteratively and the solution procedure is summarised as follows:

1) Solve u_i at iteration *n*+1 using the values of other variables at the previous iteration *n*.

2) Solve the pressure correction equation using the SIMPLE or PISO algorithm to update *p* and u_i at iteration *n*+1.

3) Solve T, σ_{ij}, q_i, m_{ijk}, R_{ij}, Δ at iteration $n+1$ using updated pressure and velocity fields.

4) Update the boundary conditions according to equations (36), (37) and (39)–(46).

5) Return to step 1 and repeat until residuals of each governing equation reaches a specified convergence criterion.

Computationally, it is more expensive to solve the R26 equations than the NSF equations but this cost is necessary to capture non-equilibrium phenomena. However, the advanced computational and numerical techniques developed over the years for conventional computational fluid dynamics can be readily adopted so that the moment method can be applied for engineering applications where non-equilibrium effects are important. In particular, in the low-speed, low Reynolds number regime where it can be costly and difficult to get meaningful statistical data from stochastic methods, the R26 equations have a significant computational advantage.

7.0   VALIDATIONS AND APPLICATIONS

As the macroscopic models are reduced from detailed kinetic theory, some kinetic information is lost during the reduction process. Two important features of solutions to the Boltzmann equation is that the distribution function, *f*, is non-negative and the solution must satisfy the *H*-theorem [6]. However, a solution obtained from the moment equations as an approximation to *f* may not satisfy these constraints. It is proved that the linearised R13 equations naturally fulfil the *H*-theorem [37]. For full R13 and R26 moment equations, numerical analysis is required to assess the moment realizability and the *H*-theorem inequality [14]. From the engineering point of view, it is necessary to validate the macroscopic models against available kinetic data as much as possible. In this section, we will first use the linearised moment equations to obtain analytical solutions for Kramers' problem and Poiseuille flow. Numerical techniques are then used to solve the moment equations for complicated flow configurations. The analytical and numerical solutions will be compared with kinetic data for the Boltzmann equation and DSMC data to demonstrate the capability as well as the limitation of the macroscopic modelling approach.

7.1   Kramers' Problem and Knudsen Layer

The Knudsen layer is a boundary layer that bridges the wall effect and the bulk flow. Kramers' problem [38], first formulated in 1949, is the most basic configuration, where the effect of a solid wall can be investigated without additional complications found in more realistic geometries. It has been extensively studied [39–43] and it provides a useful benchmark for the development of macroscopic models. As a half-space problem, it can be readily solved by the linearised equations (70)–(75). The wall is set at $\bar{y} = 0$ and the shear stress, $\bar{\sigma}_{xy}$, is constant so there is no pressure gradient in the x direction. The mean free path, λ, is chosen as the characteristic length, L, so that $\lambda/L=1$. Integration of equation (71) gives the velocity profile as:

$$\bar{u} = -\sqrt{\frac{\pi}{2}}\bar{\sigma}_{xy}\bar{y} - \frac{2}{5}\bar{q}_x - \bar{m}_{xyy} + A, \tag{85}$$

where A is an integration constant determined by the wall boundary conditions. The superposition of the velocity contributions from $\bar{\sigma}_{xy}$, $\bar{q}_x$ and $\bar{m}_{xyy}$ is clearly expressed by equation (85). This is an important feature that is not present in the NSF equations, in which $\bar{q}_x = 0$ and $\bar{m}_{xyy} = 0$. The expressions for $\bar{q}_x$ and $\bar{m}_{xyy}$ can be obtained from equations (72)–(74) as:

$$\bar{m}_{xyy} = C_1 \sqrt{\frac{\pi}{2}} \frac{2-\alpha}{\alpha} \bar{\sigma}_{xy} e^{-\left(1.212\sqrt{\pi/2}\,\bar{y}\right)}, \tag{86}$$

$$\bar{q}_x = 0.445 C_2 \frac{2-\alpha}{\alpha} \sqrt{\frac{\pi}{2}} \bar{\sigma}_{xy} e^{-\left(0.594\sqrt{\pi/2}\right)\bar{y}} \tag{87}$$

where C_1 and C_2 are integration constants. In the above solutions, the boundary condition that as $\bar{y} \to \infty$, $\bar{q}_x$, $\bar{m}_{xyy}$ and $\bar{R}_{xy}$ will remain finite has been used to remove the other two integration constants and the terms associated with them. The remaining integration constants, A, C_1 and C_2, are determined from the wall boundary conditions (59), (63) and (65) by

$$C_1 = -\frac{\left(0.291\alpha + 1.658\right)\alpha}{0.101\alpha^2 + 1.128\alpha + 9.0}, \tag{88}$$

$$C_2 = \frac{\left(0.639\alpha - 3.592\right)\alpha}{0.101\alpha^2 + 1.128\alpha + 9.0}, \tag{89}$$

$$A = -\frac{2-\alpha}{\alpha}\sqrt{\frac{\pi}{2}}\bar{\sigma}_{xy}\left(1 - 0.5 C_1 - 0.117 C_2\right). \tag{90}$$

Inserting equations (86)–(90) into equation (85), the final expression for velocity from the LR26 moment equations reads

$$\bar{u} = -\sqrt{\frac{\pi}{2}}\bar{\sigma}_{xy}\left[\bar{y} + \frac{2-\alpha}{\alpha}\left(C_1 e^{-\left(1.212\sqrt{\pi/2}\,\bar{y}\right)} + 0.178 C_2 e^{-\left(0.594\sqrt{\pi/2}\right)\bar{y}} - 0.5 C_1 - 0.117 C_2 + 1\right)\right]. \tag{91}$$

In the linearised R13 system (LR13), the governing differential equations (73) and (74) are replaced by the following constitutive relationships [44]:

$$\bar{m}_{xyy} = -\frac{16}{15}\frac{\lambda}{L}\sqrt{\frac{2}{\pi}}\frac{\partial\bar{\sigma}_{xy}}{\partial\bar{y}} \quad\text{and}\quad \bar{R}_{xy} = -\frac{12}{5}\frac{\lambda}{L}\sqrt{\frac{2}{\pi}}\frac{\partial\bar{q}_x}{\partial d\bar{y}}, \tag{92}$$

along with the boundary conditions (59) and (63) without the higher moments, $\bar{\psi}_{xyy}$ and $\bar{\Omega}_x$. For Kramers' problem, it is interesting to see that $\bar{m}_{xyy} = 0$ in the LR13 model. The velocity field for the LR13 equations is readily obtained as

$$\bar{u} = -\sqrt{\frac{\pi}{2}}\bar{\sigma}_{xy}\left[\bar{y} + \frac{2-\alpha}{\alpha}\left(\frac{\left(13 - 2\sqrt{10\pi}\right)\alpha + 4\sqrt{10\pi}}{\left(12 - 2\sqrt{10\pi}\right)\alpha + 4\sqrt{10\pi}} - \frac{\alpha e^{-\left(\sqrt{5\pi/18}\right)\bar{y}}}{\left(6 - \sqrt{10\pi}\right)\alpha + 2\sqrt{10\pi}}\right)\right]. \tag{93}$$

If we compare equations (91) and (93), we can see that the LR26 equations provide two exponentials to describe the Knudsen layer whilst the LR13 equations only contain one exponential.

In kinetic theory, the defect velocity and slip coefficient are often used to study how the wall affects the velocity profile [39–43]. To be consistent with the kinetic solutions obtained from the Boltzmann equation, a reference velocity defined by

$$u_o = -\sigma_{xy}\frac{\lambda}{\mu} = -\bar{\sigma}_{xy}\sqrt{\frac{\pi RT_o}{2}} \tag{94}$$

is used to scale the velocity i.e.

$$
\begin{aligned}
\tilde{u} = \frac{u}{u_o} &= \frac{u}{-\sqrt{\pi/2}\,\bar{\sigma}_{xy}\sqrt{RT_o}} = \frac{\bar{u}}{-\sqrt{\pi/2}\,\bar{\sigma}_{xy}} \\
&= \frac{-\sqrt{\pi/2}\,\bar{\sigma}_{xy}\left[\bar{y}+\dfrac{2-\alpha}{\alpha}\left(C_1 e^{-\left(1.212\sqrt{\pi/2}\,\bar{y}\right)}+0.178 C_2 e^{-\left(0.594\sqrt{\pi/2}\right)\bar{y}}-0.5C_1-0.117C_2+1\right)\right]}{-\sqrt{\pi/2}\,\bar{\sigma}_{xy}} \\
&= \bar{y}+\frac{2-\alpha}{\alpha}\left(C_1 e^{-\left(1.212\sqrt{\pi/2}\,\bar{y}\right)}+0.178 C_2 e^{-\left(0.594\sqrt{\pi/2}\right)\bar{y}}-0.5C_1-0.117C_2+1\right).
\end{aligned}
\tag{95}
$$

A defect velocity, u_d, is defined by [40, 43]

$$u_d = \bar{y}+\zeta-\tilde{u} \tag{96}$$

and the slip coefficient, ζ, is determined by

$$\lim_{\bar{y}\to\infty} u_d = 0. \tag{97}$$

From the above condition, the expression of ζ for the LR26 moment equations can be written as

$$\zeta = \frac{2-\alpha}{\alpha}\left(1-0.5C_1-0.117C_2\right) \tag{98}$$

and the defect velocity is expressed by

$$u_d = -\frac{2-\alpha}{\alpha}\left(C_1 e^{-1.212\sqrt{\pi/2}\,\bar{y}}+0.178 C_2 e^{-0.594\sqrt{\pi/2}\,\bar{y}}\right). \tag{99}$$

Similarly, we can obtain the defect velocity and slip coefficient for the LR13 equations, respectively, as

$$\zeta = \frac{2-\alpha}{\alpha}\left[\frac{\left(13-2\sqrt{10\pi}\right)\alpha+4\sqrt{10\pi}}{\left(12-2\sqrt{10\pi}\right)\alpha+4\sqrt{10\pi}}\right], \tag{100}$$

$$u_d = \frac{2-\alpha}{\alpha}\left[\frac{\alpha e^{-\sqrt{5\pi/18}\,\bar{y}}}{\left(6-\sqrt{10\pi}\right)\alpha+2\sqrt{10\pi}}\right]. \tag{101}$$

Figure 4 presents the analytical solutions of the defect velocity in the Knudsen layer from the moment equations in comparison with the computational results from the three kinetic models investigated by Siewert [43], i.e. the BGK model, the Williams model (the collision frequency is proportional to the magnitude of the velocity), and the hard sphere model. For the case of $\alpha = 0.9$, diffusive reflection from the wall dominates. The BGK kinetic model produces the largest defect velocity in the Knudsen layer, particularly close to the wall ($\bar{y} < 0.5$). In contrast, the results from the Williams and hard sphere models

are in close agreement with each other. The analytical solution from the LR26 equations generally lies between the three models and, beyond $\bar{y} = 0.5$, is in close agreement with the BGK model. However, at the wall, all kinetic models predict a higher defect velocity. Conversely, the solution obtained from the LR13 equations underpredicts the defect velocity significantly, as shown in Figure 4(a). As the LR13 system involves fewer equations and boundary conditions than the LR26 system, less kinetic information is preserved in the LR13 model. Clearly the combination of two exponentials with different widths produces an improved Knudsen layer velocity profile. It is expected that more moments and their governing equations would generate more exponentials with different widths to recover the full kinetic information. As the value of the accommodation coefficient decreases, the previous observations remain valid although, as expected, the defect velocity increases, as shown in Figure 4(b). In this case, where $\alpha = 0.1$, specular wall reflection dominates. The results shown in Figure 4 illustrate that the LR26 equations work well for walls exhibiting either diffusive or specular reflection.
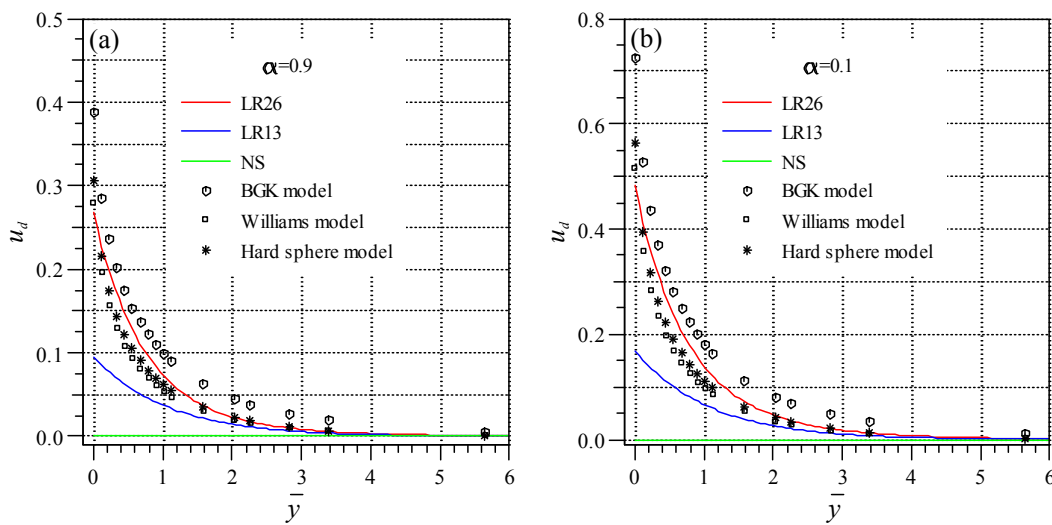
Figure 4: Defect velocity profile for Kramers' problem: comparison between the moment equation solutions (lines) and kinetic theory (symbols) [43]. (Note: The original data in Ref [43] are presented in terms of the mean free path defined by $l = \left(2/\sqrt{\pi}\right)\lambda$. . The data were converted to be consistent with the present definition of the mean free path, λ.).

Equation (85) illustrates that the velocity in the Knudsen layer consists of contributions from $\bar{\sigma}_{xy}$, $\bar{q}_x$, and $\bar{m}_{xyy}$. For the LR13 equations, $\bar{m}_{xyy} = 0$, there is no mechanism for $\bar{m}_{xyy}$ to contribute; so the Knudsen layer is derived solely from the tangential heat flux, $\bar{q}_x$. In the NSF system, $\bar{q}_x$ and $\bar{m}_{xyy}$ are not present, so there is no Knudsen layer. If we take the distance to the wall as the characteristic length, the corresponding Knudsen number is the reciprocal of $\bar{y}$. Figure 4 suggests that the LR26 and LR13 equations can capture the Knudsen layer velocity in a half space configuration for a Knudsen number equal to 2 $\left(\bar{y} = 0.5\right)$ and 0.5 $\left(\bar{y} = 2\right)$, respectively. However, in confined geometries, Knudsen layers from opposite walls will overlap [14] and, for the R26 and R13 equations, this will reduce the value of the Knudsen number to 1 and 0.25, respectively. These results provide a clear indication that the higher moment equations can be used in the early transition regime with good accuracy to account for the wall effect on flows in MEMS.

7.2   Planar Poiseuille Flow and Knudsen Minimum

Channels are the most frequently encountered geometry in MEMS. Planar Poiseuille flow driven by a small pressure gradient is another classic case often used to check the validity of any proposed macroscopic models. The distance between the plates is chosen as the characteristic length, L, so that the Knudsen number,

$$Kn = \frac{\lambda}{L} . \tag{102}$$

The two plates have been set at $y = \pm L/2$, i.e., $\overline{y} = \pm 1/2$. Symmetry boundary conditions are applied at $\overline{y} = 0,$ and the flow is driven by a constant pressure gradient

$$\frac{\partial \overline{p}}{\partial \overline{x}} = -\xi . \tag{103}$$

From equation (70), the shear stress can be expressed by

$$\overline{\sigma}_{xy} = \xi \overline{y} . \tag{104}$$

Integration of equation (71) gives:

$$\overline{u} = -\sqrt{\frac{\pi}{2}} \frac{\xi}{2Kn} \overline{y}^2 - \overline{m}_{xyy} - \frac{2}{5} \overline{q}_x + B , \tag{105}$$

in which B is an integration constant. Again, it is clearly shown from equation (105) that the velocity profile in the confined geometry has contributions from not only σ_{xy}, but also from m_{xyy} and q_x, which can be obtained from equations (72)-(74) as:

$$m_{xyy} = -\frac{16}{15} \xi Kn \sqrt{\frac{2}{\pi}} + C_3 \xi \cosh\left(\frac{1.212\sqrt{\pi/2}}{Kn} \overline{y} \right) , \tag{106}$$

$$q_x = -\frac{3}{2} \xi \sqrt{\frac{2}{\pi}} Kn + C_4 \xi \cosh\left(0.594 \frac{\sqrt{\pi/2}}{Kn} \overline{y} \right) \tag{107}$$

where C_3 and C_4 are the integration constants, along with B, are determined by the boundary conditions (59), (63) and (65) as:

$$B = \left(\frac{1}{8Kn} \sqrt{\frac{\pi}{2}} - \frac{5}{6} \sqrt{\frac{2}{\pi}} Kn + \frac{2-\alpha}{2\alpha} \sqrt{\frac{\pi}{2}} + 0.264 C_4 \cosh\left(\frac{0.372}{Kn} \right) + \frac{C_3}{2} \cosh\left(\frac{0.759}{Kn} \right) \right) \xi \tag{108}$$

$$C_3 = \frac{E_2 F_3 - E_3 F_2}{E_1 F_2 - F_1 E_2} \quad \text{and} \quad C_4 = -\frac{E_1 F_3 - F_1 E_3}{E_1 F_2 - F_1 E_2} \tag{109}$$

with

$$
\begin{cases}
E_1 = \dfrac{5}{18}\cosh\left(\dfrac{0.759}{Kn}\right), \quad E_2 = 0.968\cosh\left(\dfrac{0.372}{Kn}\right) + 0.782\sinh\left(\dfrac{0.372}{Kn}\right)\dfrac{2-\alpha}{\alpha}, \\[2mm]
F_1 = \dfrac{2}{3}\cosh\left(\dfrac{0.759}{Kn}\right) + 0.517\sinh\left(\dfrac{0.759}{Kn}\right)\dfrac{2-\alpha}{\alpha}, \\[2mm]
F_2 = 0.437\cosh\left(\dfrac{0.372}{Kn}\right) + 0.402\sinh\left(\dfrac{0.372}{Kn}\right)\dfrac{2-\alpha}{\alpha}, \\[2mm]
E_3 = -\dfrac{2-\alpha}{\alpha}\dfrac{5}{36}\sqrt{\dfrac{\pi}{2}} - \dfrac{35}{27}\sqrt{\dfrac{2}{\pi}}Kn, \quad F_3 = -\dfrac{2-\alpha}{6\alpha}\sqrt{\dfrac{\pi}{2}} - \dfrac{10}{9}\sqrt{\dfrac{2}{\pi}}Kn.
\end{cases}
\tag{110}
$$

Substituting equations (106)-(108) into equation (105), the velocity profile of planar Poiseuille flow is obtained as

$$
\begin{aligned}
\bar{u} &= \dfrac{\xi}{2Kn}\sqrt{\dfrac{\pi}{2}}\left(\dfrac{1}{4} - \bar{y}^2\right) + \sqrt{\dfrac{\pi}{2}}\xi\left(\dfrac{5}{3}\dfrac{Kn}{\pi} + \dfrac{2-\alpha}{2\alpha}\right) + C_3\xi\left[\dfrac{1}{2}\cosh\left(\dfrac{0.759}{Kn}\right) - \cosh\left(\dfrac{1.212\sqrt{\pi/2}}{Kn}\bar{y}\right)\right] \\[2mm]
&+ C_4\xi\left[0.264\cosh\left(\dfrac{0.372}{Kn}\right) - \dfrac{2}{5}\cosh\left(\dfrac{0.594\sqrt{\pi/2}}{Kn}\bar{y}\right)\right].
\end{aligned}
\tag{111}
$$

In order to compare with the linearized Boltzmann solution [7, 45], a reference velocity,

$$
u_o = \xi\sqrt{2RT_o}
\tag{112}
$$

is used to renormalize the velocity as

$$
\begin{aligned}
\tilde{u} &= \dfrac{u}{u_o} = \dfrac{\sqrt{RT_o}\bar{u}}{\xi\sqrt{2RT_o}} = \dfrac{\bar{u}}{\xi\sqrt{2}} \\[2mm]
&= \dfrac{\sqrt{\pi}}{4Kn}\left(\dfrac{1}{4} - \bar{y}^2\right) + \dfrac{\sqrt{\pi}}{2}\left(\dfrac{5}{3}\dfrac{Kn}{\pi} + \dfrac{2-\alpha}{2\alpha}\right) + \dfrac{C_3}{\sqrt{2}}\left[0.5\cosh\left(\dfrac{0.759}{Kn}\right) - \cosh\left(\dfrac{1.212\sqrt{\pi/2}}{Kn}\bar{y}\right)\right] \\[2mm]
&+ \dfrac{C_4}{\sqrt{2}}\left[0.264\cosh\left(\dfrac{0.372}{Kn}\right) - \dfrac{2}{5}\cosh\left(\dfrac{0.594\sqrt{\pi/2}}{Kn}\bar{y}\right)\right].
\end{aligned}
\tag{113}
$$

The normalised mass flow rate of planar Poiseuille flow, Q, can be obtained by the integration of equation (113) over the channel width as

$$
\begin{aligned}
Q &= \int_{1/2}^{1/2}\tilde{u}\,d\bar{y} \\[2mm]
&= \dfrac{\sqrt{\pi}}{24Kn} + \dfrac{\sqrt{\pi}}{2}\left(\dfrac{5}{3}\dfrac{Kn}{\pi} + \dfrac{2-\alpha}{2\alpha}\right) + \dfrac{C_3}{\sqrt{2}}\left[0.5\cosh\left(\dfrac{0.759}{Kn}\right) - 1.317Kn\sinh\left(\dfrac{0.759}{Kn}\right)\right] \\[2mm]
&+ \dfrac{C_4}{\sqrt{2}}\left[0.264\cosh\left(\dfrac{0.372}{Kn}\right) - 1.075Kn\sinh\left(\dfrac{0.372}{Kn}\right)\right].
\end{aligned}
\tag{114}
$$

Similarly, we can obtain the velocity profiles from the LR13 equations as

$$\tilde{u} = \frac{\sqrt{\pi}}{4Kn}\left(\frac{1}{4} - \bar{y}^2\right) + \frac{\sqrt{\pi}}{2}\left(\frac{5Kn}{3\pi} + \frac{2-\alpha}{2\alpha}\right) + \frac{C_5}{5\sqrt{2}}\left[\cosh\left(\frac{\sqrt{10\pi}}{12Kn}\right) - 2\cosh\left(\frac{\sqrt{10\pi}}{6Kn}\bar{y}\right)\right], \qquad (115)$$

in which the constant C_5 is determined from the boundary conditions as:

$$C_5 = \frac{5}{24}\frac{\sqrt{2}\left(3\pi\frac{2-\alpha}{\alpha} + 56Kn\right)}{\pi\frac{2-\alpha}{\alpha}\sqrt{10}\sinh\left(\frac{\sqrt{10\pi}}{12Kn}\right) + 6\sqrt{\pi}\cosh\left(\frac{\sqrt{10\pi}}{12Kn}\right)}. \qquad (116)$$

The normalised flow rate obtained from the LR13 equations is:

$$Q = \frac{\sqrt{\pi}}{24Kn} + \frac{\sqrt{\pi}}{2}\left(\frac{5Kn}{3\pi} + \frac{2-\alpha}{2\alpha}\right) + \frac{C_5}{5\sqrt{2}}\left[\cosh\left(\frac{\sqrt{10\pi}}{12Kn}\right) - \frac{12}{5}\sqrt{\frac{10}{\pi}}\sinh\left(\frac{\sqrt{10\pi}}{12Kn}\right)Kn\right]. \qquad (117)$$

The velocity profiles calculated from equations (113) and (115) from the LR26 and LR13 moment equations, respectively, are presented in Figure 5 at a range of Knudsen numbers in comparison with the solution from the linearised Boltzmann equation [7]. At Kn=0.113, which is just beyond the slip-flow regime, both extended hydrodynamic models predict similar values of velocity and are all close to the solution obtained from the Boltzmann equation, as shown in Figure 5(a). The LR13 equations underpredict while the R26 equations slightly overpredict the maximum velocity. However, as the value of Kn increases and the flow enters the transition regime, the LR13 equations overpredict the slip velocity significantly. In contrast, the velocity fields predicted by the LR26 equations compare very well to the solution obtained from the Boltzmann equation for both Kn=0.226 and 0.451, as shown in Figures 5(b) and (c). The velocity-slip predicted by the LR26 equations is in reasonable agreement with the value predicted by the Boltzmann equation but discrepancies in the bulk flow begin to show at Kn=0.903, Figure 5(e), and differ at Kn=1.128, as shown in Figure 5(f).
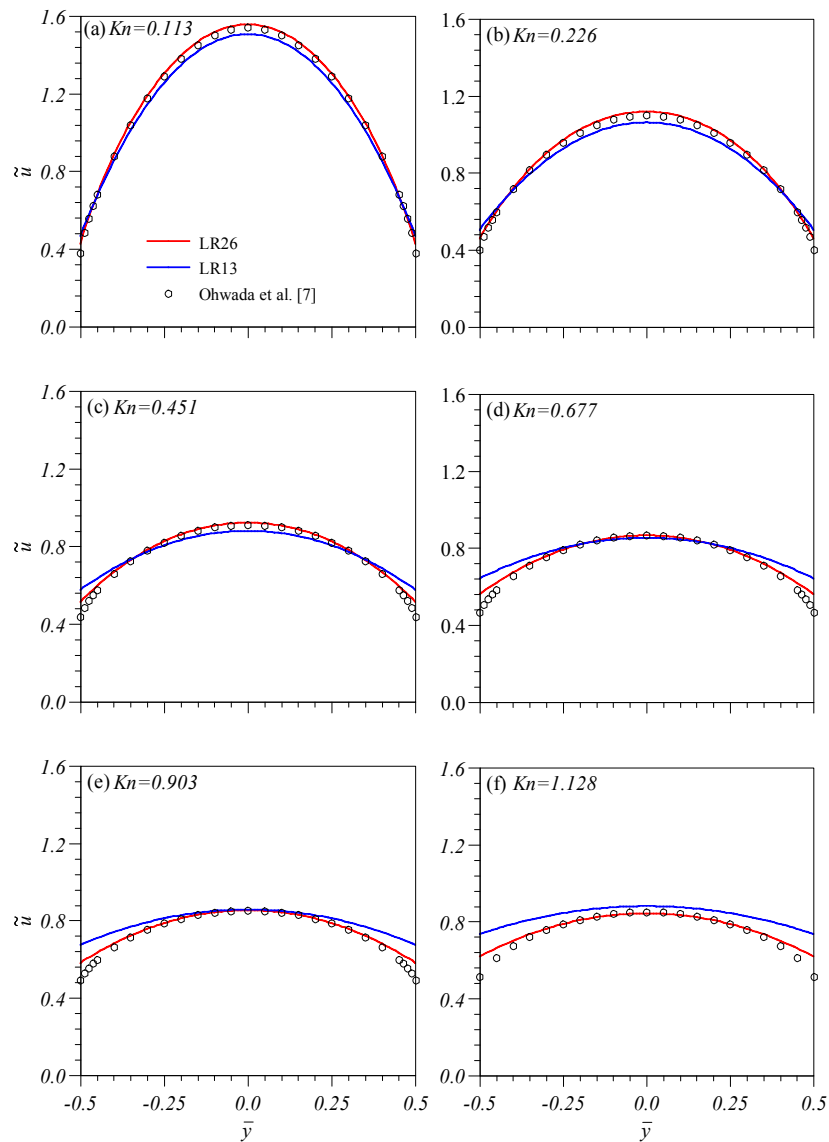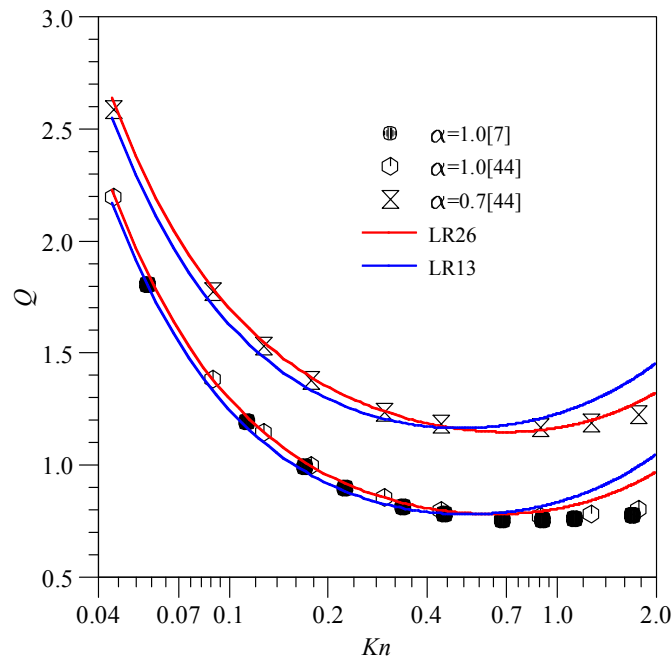
**Figure 5: Comparison of velocity profiles of pressure-driven Poiseuille flow at different
values of Knudsen number between the linearized moment equation
solution and the linearised Boltzmann equation solution [7].**

The accurate prediction of the flow rate in a micro-channel is important in the design of micro-devices. To get the flow rate correct, it is essential that the predicted velocity profile is correct. In contrast, the correct prediction of the flow rate cannot guarantee the correct velocity profile. Figure 6 shows the predicted mass flow rates by the LR13 and LR26 equations in comparison to the solution obtained from the Boltzmann equation [7, 44] at two different accommodation coefficients. When $Kn < 0.1$ in the slip regime, the flow rates predicted by both models are close to the solution obtained from the Boltzmann equation. As the value of Kn increases, non-equilibrium effects gradually enter the central flow region, the LR26 equations follow the solution obtained from the Boltzmann equation reasonably well until Kn reaches about 1.5. As shown in Figure 6, the LR26 equations predict a Knudsen minimum at the value of Kn predicted by the Boltzmann equation for both $\alpha = 0.7$ and 1.0. The R13 equations are close to the Boltzmann solution up to $Kn \approx 0.4$, particularly for the lower value of α. They can also predict a Knudsen minimum but at a value of Kn smaller than that observed by the Boltzmann equation.

**Figure 6: Comparison of mass flow rate of pressure-driven Poiseuille flow at different
values of Knudsen number between the linearized moment equation
solution and the linearised Boltzmann equation solution [7, 44].**

One of the interesting effects of rarefaction in Poiseuille flow revealed by kinetic theory is the presence of heat flow in a channel without any temperature gradient [7]. This phenomenon is also captured by the LR26 moment equations. The tangential heat flux is caused by the pressure gradient and the Knudsen layer contribution as expressed by the first and second terms in the right-hand side of equation (107), respectively. When the Knudsen number is small, heat flows in the opposite direction to the mass flow at the centre of the channel but, close to the wall, it is in the same direction as the mass flow, as indicated in Figure 7. However, as the Knudsen number increases, heat flow is always in the opposite direction to the mass flow. This is a high-order rarefaction effect which is clearly not embedded in the NSF equations.
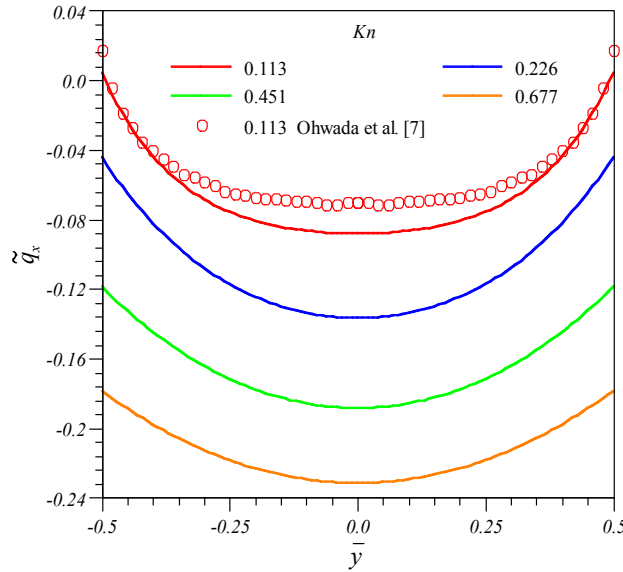
Figure 7: Tangential heat flux of pressure-driven Poiseuille flow at different values of *Kn*
with fully diffusive walls. Lines: the LR26, Symbols: the linearised Boltzmann equation
[7]. $\tilde{q}_x$ is the normalised tangential heat flux by $\tilde{q}_x = q_x \big/ \left(p_o \sqrt{2RT} \right) = \overline{q}_x \big/ \sqrt{2}$.

7.3   Stokes' Second Problem and Oscillatory Planar Couette Flow

Many MEMS devices contain oscillating parts where air (viscous) damping plays an important role. To understand the damping mechanisms, it is essential to consider non-equilibrium or rarefaction effects. In oscillatory flows, additional non-equilibrium effects can arise if there are an insufficient number of intermolecular collisions during one cycle of the oscillation. To quantify the extent of rarefaction in this respect, Sharipov and Kalempa [45, 46] introduced a rarefaction parameter, θ, as

$$\theta = \frac{\eta}{\omega}, \tag{118}$$

in which ω and η are the oscillation and the intermolecular collision frequency, respectively. By analogy with the *spatial* Knudsen number, *Kn*, which is based upon a typical length scale, it is convenient to adopt a *temporal* Knudsen number, Kn_t, which is defined as the reciprocal of θ, to express the extent of non-equilibrium from the aspect of time scale [47], i.e.

$$Kn_t = \frac{1}{\theta} = \frac{\omega}{\eta} \ . \tag{119}$$

The intermolecular collision frequency, η, can be estimated by p/μ [6]. When $Kn_t \ll 1$, many intermolecular collisions occur during one cycle of the oscillation so that unsteadiness has little effect on the flow to approach the equilibrium state. On the other hand, in the regime where $Kn_t \gg 1$, very few intermolecular collisions occur during one cycle of the oscillation. The intermolecular collisions can be neglected and the free molecular formulation of the Boltzmann equation can be used. In a system where $Kn_t \sim 1$, the number of the intermolecular collisions is not sufficiently large for the flow to reach an equilibrium state during one oscillation cycle. Rarefaction effects have to be taken into account when modeling flows in this regime.

Analytical solutions of the Navier-Stokes equation for Stokes' second problem and oscillatory planar Couette flow, with either first-order or second-order velocity-slip boundary conditions, can be found in the works of Sharipov and Kalempa [45, 46], Park et al. [48] and Hadjiconstantinou [49]. Emerson et al. [50] studied nonplanar oscillatory Couette flow in the entire range of Knudsen number. The analytical solutions for the LR13 and LR26 moment equations can also be obtained; they are a linear combination of 4 and 6 exponentials with different widths for the LR13 and LR26 equations, respectively. However, the expressions for the coefficients and the widths are rather complicated and cumbersome. It is therefore more convenient to solve the one dimensional LR13 and LR26 equations numerically [47]. Equations (70) –(74) can readily be solved using a central difference scheme to discretize the spatial derivatives and a second-order Crank-Nicholson method for the temporal terms.

Stokes' second problem is a half space configuration with the oscillating wall located at $y = 0$. The mean free path, λ, is chosen as the characteristic length so that λ/L in equations (70) – (75) is equal to 1. The gas molecules are assumed to diffusively reflect from the oscillating wall and the gradients of all variables are equal to zero at the open end of the solution domain. To solve the system of equations, 200 to 400 equi-spaced grid points are used depending on the oscillation frequency. For oscillatory planar Couette flow, the lower plate is located at $y = 0$ and remains stationary. The upper plate, ($y = L$), oscillates at a fixed frequency. The gap between the two plates, L, is chosen as the characteristic length scale, so that λ/L in equations (70) – (75) is equal to Kn. The flow is solved with 200 grid points across the one-dimensional domain. For both configurations, the moving wall oscillates sinusoidally according to

$$u_o = u_w \sin(\omega t), \tag{120}$$

where ω and u_w are the oscillating frequency and magnitude of the wall, respectively, and u_o is the instantaneous wall velocity. The numerical time interval is taken as one hundredth of a period. The accommodation coefficients of the lower and upper walls are assigned a value of unity. All computations are impulsively started with zero velocity everywhere and 50 to 100 periods are computed to remove the quiescent initial effects and to ensure that a quasi-steady periodic state is reached. Computed results for the macroscopic models are then compared with data from kinetic theory to assess their validity.

7.3.1 Stokes' Second Problem

The dynamic velocity profiles from the linearised moment equations at four points in time, corresponding to $\omega t = 0$, $\pi/2$, π, $3\pi/2$, are presented in Figure 8. At the lower value of Kn_t equal to 0.1, where many intermolecular collisions occur during one cycle of oscillation, the results from both extended continuum models are nearly identical, as shown in Figure 8(a). Analogous to the classification for steady flow, we can denote the regime of $Kn_t < 0.1$ as the hydrodynamic regime. As Kn_t increases to 0.5, in Figure 8(b), the solutions from the LR13 and LR26 equations start to deviate from each other. At Kn_t equal to unity, well into the transition regime, the velocity profiles from the LR13 equations are significantly different from those of the LR26 equations not only in the region close to the wall but also in the bulk flow, as indicated in Figure 8(c). The LR13 equations predict a larger slip velocity than the LR26 equations which is due to the LR13 equations lacking a proper mechanism to capture the Knudsen layer velocity profile near the wall [21] and the oscillation aggravates the situation. In general, the slip velocity increases as Kn_t increases so that the velocity on the wall reduces.

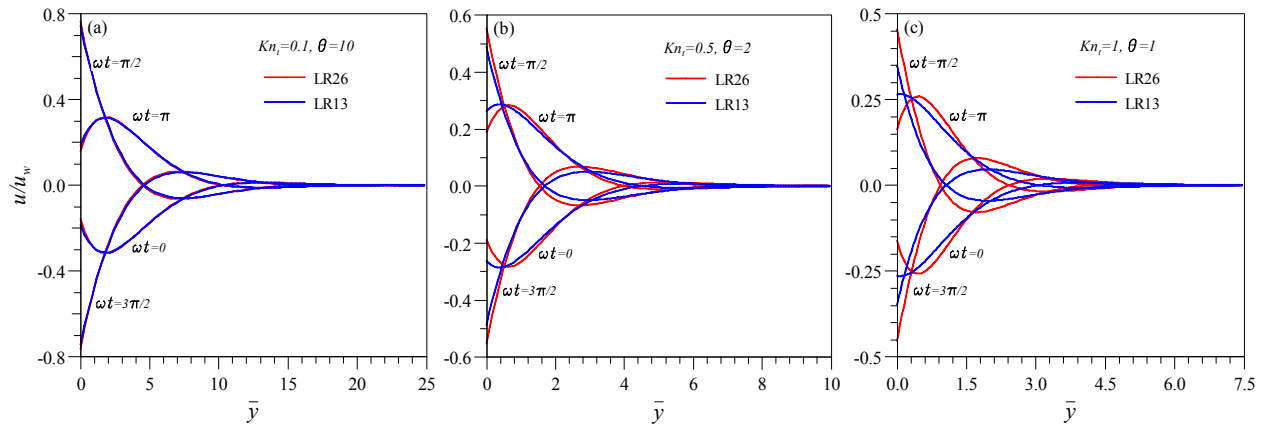**Figure 8: Dynamic velocity profiles of Stokes' second problem from the extended
hydrodynamic models at four different times. Adapted from Ref. [47].**

The predicted values of the velocity amplitude at the wall from each of the hydrodynamic models are plotted against Kn_t in Figure 9(a) and compared to the kinetic data from the linearised BGK model [45]. The Navier-Stokes equations always under-predict the velocity amplitude on the wall even in the hydrodynamic region. Both extended macroscopic models improve the prediction of u_m on the wall significantly, as shown in Figure 9(a), up to $Kn_t = 0.5$ with the LR26 equations showing better agreement than the LR13 equations.
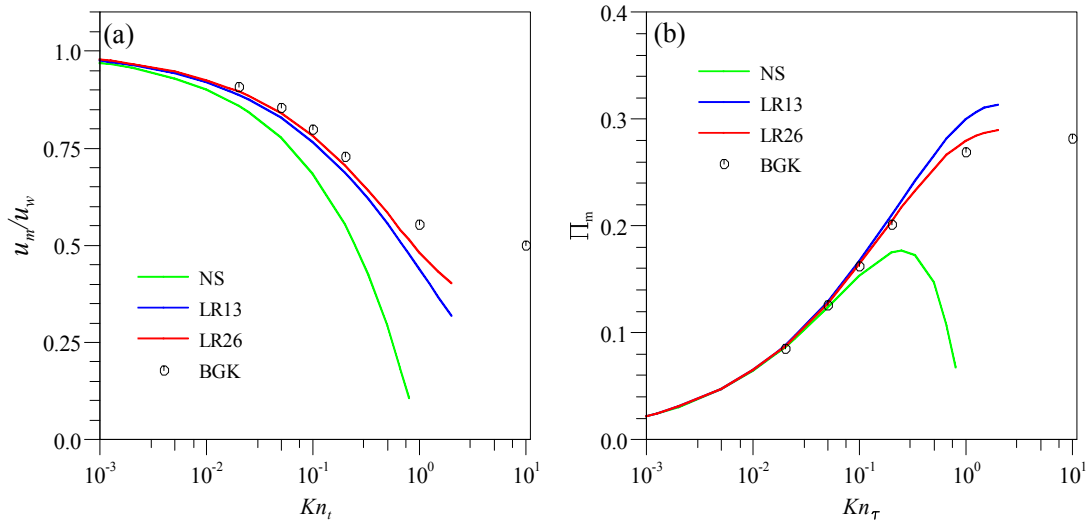
**Figure 9: Predicted velocity and shear stress amplitudes on the wall of Stokes'
second problem from macroscopic models in comparison with
the data from the linearised BGK kinetic equation [45].**

To compare with kinetic data [45], the shear stress, σ_{xy}, is renormalised as

$$\Pi = \frac{\sigma_{xy}}{2p_o} \frac{\sqrt{2RT_o}}{u_w} \tag{121}$$

The predicted value of the shear stress amplitude on the wall, Π_m, from the hydrodynamic models and kinetic theory are presented in Figure 9(b). In the hydrodynamic regime, where $Kn_t < 0.05$, all the

hydrodynamic models predict similar values of Π_m on the wall and are in good agreement with kinetic theory. When Π_m is exceeds 0.1, the NS equations start to underestimate Π_m, while both the LR13 and LR26 equations are still able to follow the kinetic data. The LR13 equations tend to overpredict Π_m when $Kn_t > 0.5$.

The corresponding velocity and shear stress phases on the wall, φ_u and φ_P, as defined by Sharipov and Kalempa [45], are presented in Figure 10. The velocity phase, φ_u, has a maximum value in the transition regime as shown in Figure 10(a). The NS and LR13 equations fail to predict any maximum value. In contrast, the LR26 equations predict a maximum value of φ_u, but the value is larger than that from kinetic theory. In general, the agreements of φ_u between the hydrodynamic models and kinetic theory are not satisfactory in the slip and transition regimes, although the LR26 model improves the prediction substantially. However, it should be pointed out that the maximum value of φ_u on the wall is less than 4% of one period. Conversely, all extended hydrodynamic models predict the shear stress phase, φ_P, very well up to $Kn_t = 1$, as illustrated in Figure 10(b). The NS equations underestimate the value of φ_P, from a very low value of Kn_t.
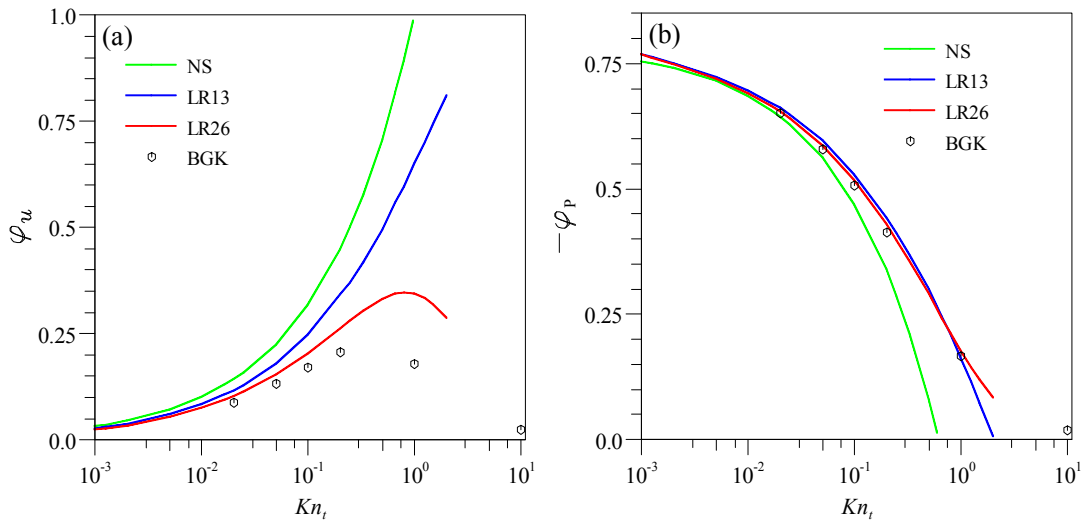

**Figure 10: Predicted velocity and shear stress phases on the wall of Stokes'
second problem from macroscopic models in comparison with the data
from the linearised BGK kinetic equation [45]. Adapted from Ref. [47].**

7.3.2   Oscillatory Planar Couette Flow

For oscillatory planar Couette flow under rarefied conditions, non-equilibrium effects will arise from both the separation distance and the oscillation of the walls. Therefore, both Knudsen numbers, Kn and Kn_t, defined upon a length and time scale, respectively, are required to measure the extent of non-equilibrium. Traditionally, the Stokes number, S, defined by

$$S = \sqrt{\frac{\rho_o \omega L^2}{\mu}} , \tag{122}$$

is often used to characterize the balance between the unsteady and viscous effects [48, 49]. To reflect non-equilibrium effects due to the oscillation, the temporal Knudsen number, Kn_t, needs to be assessed to measure the oscillatory effect on the flow, which is related to Kn and S through

$$Kn_t = \frac{2}{\pi}\left(SKn\right)^2.$$

(123)

Equation (123) indicates that Kn_t is proportional to the square of the product of Kn and S. Increasing either Kn or S can lead to a significant increase in the value of Kn_t.

Figure 11 shows the velocity amplitude, u_m, between the two walls for oscillatory planar Couette flow. Results at different values of Kn and Kn_t in the early transition regime are compared with the DSMC data [48] and the solution of the linearised BGK equation [46]. For $Kn < 0.1$, the velocity amplitudes from the LR13 and LR26 equations agree with both DSMC data and kinetic theory up to $Kn_t = 1$. When $Kn = 0.5$ and $Kn_t = 0.16$, the LR26 equations are in good agreement with the DSMC data. However, when $Kn = 1$ and $Kn_t = 0.64$, the LR26 equations can capture the velocity amplitude reasonably well but the LR13 equations cannot follow the DSMC data in the whole domain, as illustrated in Figure 11(a). For the case with $Kn = 0.886$ and $Kn_t = 1$, both the LR26 and LR13 equations fail to capture the velocity amplitude correctly, as indicated in Figure 11(b).
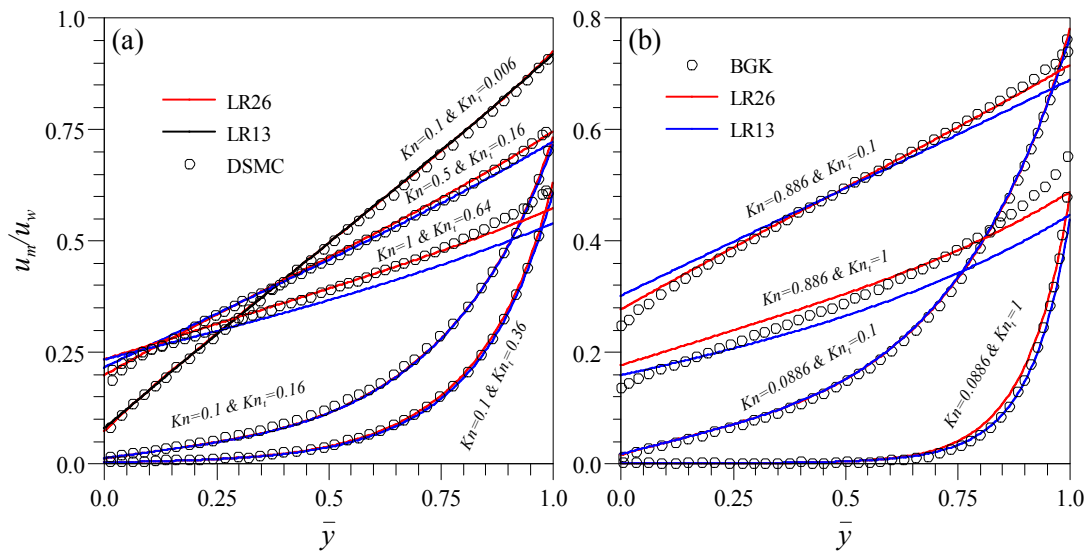
Figure 11: Normalised velocity amplitude of oscillatory planar Couette flow. Lines are from the macroscopic models. (a) Symbols are the DSMC data are digitised from Park et al. [48]. (b) Symbols are the linearised BGK data are digitised from Sharipov and Kalempa [46]. Adapted from Ref. [47].

One of the unique features in one-dimensional steady-state Couette flow is the constant shear stress across the whole domain at any value of Kn, even inside the Knudsen layer. However, this feature no longer exists when one of the plates oscillates. The amplitude of the shear stress is therefore presented in Figure 12. When both Kn and Kn_t are small, the extended hydrodynamic models agree with kinetic theory, but when these Knudsen numbers are large, the discrepancies between them are very noticeable. The complex interplay of the length and time scales exacerbates the capabilities of the macroscopic equations to capture the non-equilibrium effects at high values of either Kn or Kn_t.
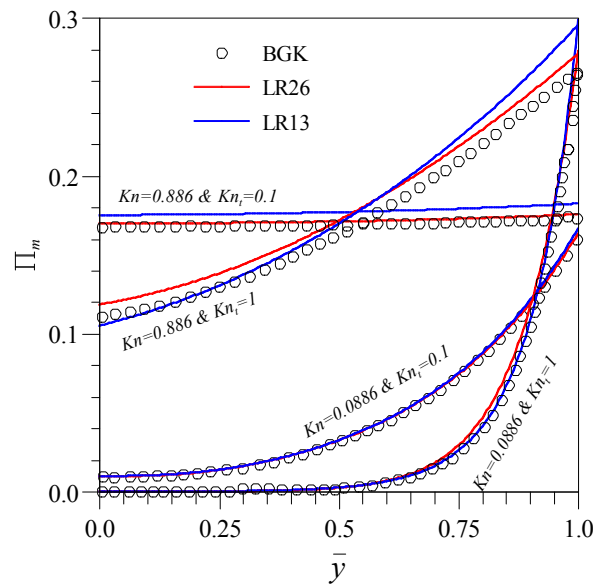
Figure 12: Normalised shear stress amplitude of the oscillatory planar Couette flow. Lines are from the macroscopic models. Symbols are the linearised BGK data are digitised from Sharipov and Kalempa [46]. Adapted from Ref. [47].

The velocity and shear stress phases, φ_u and φ_P, of oscillatory planar Couette flow are presented in Figure 13. When $Kn = 0.0886$ and $Kn_t = 0.1$, the Stokes number, S, is equal to 4.473. The LR13 and LR26 equations predict both φ_u and φ_P in excellent agreement with kinetic theory [46]. For $Kn = 0.0886$ and $Kn_t = 1$, the Stokes number reduces to 1.415. Although the LR26 equations are not able to predict u_m and Π_m very well for this particular case, as shown in Figures 11(b) and 12, they do capture the phases, φ_u and φ_P, quite accurately in comparison with the kinetic data, as indicated in Figure 13. In contrast, when $Kn = 0.0886$ and $Kn_t = 1$, both the LR13 and LR26 equations are able to predict the velocity and shear stress amplitudes correctly, as shown in Figure 11(b), but fail to predict the corresponding phases. The LR26 equations manage to follow the kinetic data within one quarter of L away from the oscillating wall but then start to overpredict φ_u and φ_P as we move further away from the moving wall, as indicated in Figure 13. The Stokes number for this case is very high, equal to 14.14. At such a large Stokes number, inertia plays a major role in the flow dynamics. An analysis of the velocity amplitudes shown in Figure 11(b) indicates that the penetration depth for this case ($Kn = 0.0886$, $Kn_t = 1$) is $0.38L$ away from the oscillating wall. The lower stationary wall hardly feels the any effect from the motion of the upper wall. It is interesting to see that the LR26 equations can predict φ_u and φ_P, within the Stokes layer while the LR13 equations fail to follow the trend of φ_u and φ_P, throughout the whole domain.
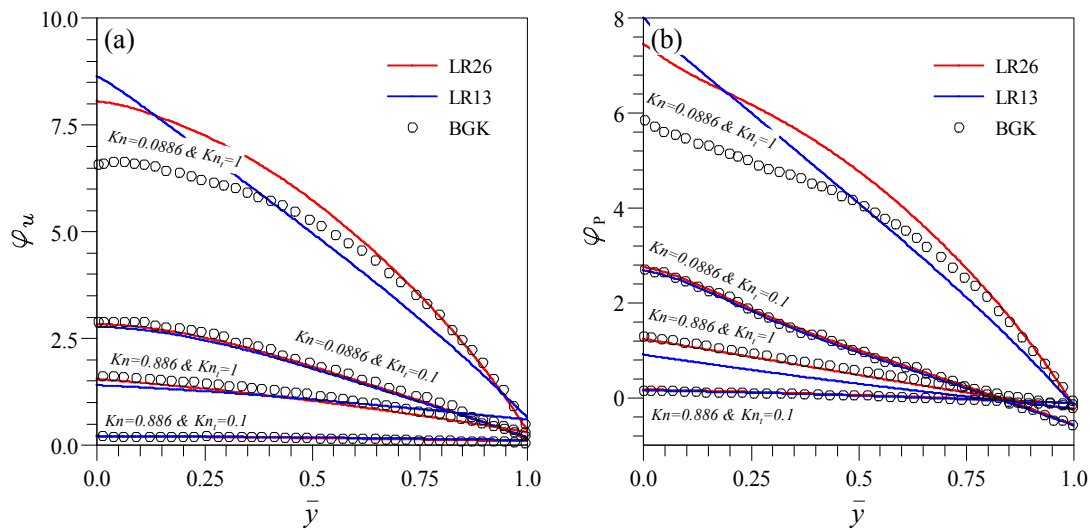
**Figure 13: Velocity and shear stress phases of oscillatory planar Couette flow. Lines are
from the macroscopic models. Symbols are the linearised BGK data digitised
from Sharipov and Kalempa [46]. Adapted from Ref. [47].**

7.4   Micro Driven Cavity Flow

The driven cavity problem is a well known benchmark problem for testing and verifying continuum
solvers [51]. The problem geometry is simple and two-dimensional, yet the flow pattern and heat transfer
in the cavity are encountered in many engineering applications. However, few studies [52-54] have been
carried out to examine the mass and heat flow patterns in a driven cavity for non-equilibrium gas flows.
Recently, John et al. [55] performed a series of DSMC simulation of gas flow in a micro lid-driven cavity
for a range of Knudsen number, Reynolds number and Mach number. The simulation results reveal
interesting non-equilibrium phenomena in the cavity and provide useful data to benchmark the extended
hydrodynamic equations.

The configuration of the square driven cavity, of size *L*, is shown in Figure 14. The notations A, B, C, and
D shown in the figure denote the four corners of the cavity. The top lid moves with a fixed tangential
velocity U_w in the positive *x* direction, and the other walls are stationary. The wall temperature is set to the
reference temperature, i.e., T_w = 273 K. Any variation in Knudsen number is achieved by changing the
density conditions in the cavity, i.e., the reference pressure p_o. The R26 moment equations discritised on a
129x129 uniform grid are numerically solved for a range of Knudsen numbers in the slip and early
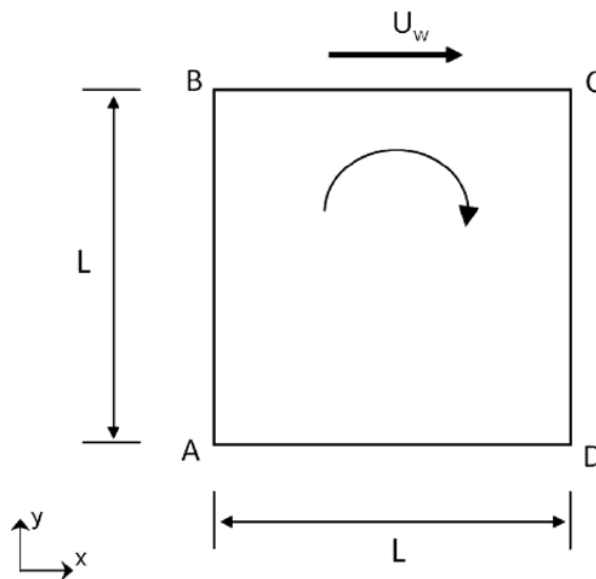transition regimes in comparison with the DSMC data.

Figure 14: Configuration of lid-driven cavity.

One of the interesting phenomena in a driven cavity under non-equilibrium condition is the gas temperature distribution and heat flux direction. Shown in Figure 15(a) is the DSMC simulation of heat flux stream traces overlaid on temperature contours at $Kn = 0.2$ with $U_w = 10$ m/s. From the temperature contours, a cold region is found toward the left corner of the cavity, whereas a hot region is observed toward the right corner of the cavity. More interestingly, it is noted that the direction of heat flow is generally from the cold to the hot region, as illustrated by the heat flux streamlines. This represents a counter-gradient heat flux made possible by the rarefied flow conditions. Under non-equilibrium flow conditions, various factors such as expansion cooling, viscous heat generation, compressibility, and thermal creep could significantly affect flow and heat transfer. For the driven cavity case, an expansion cooling (gas temperature T less than wall temperature T_w) occurs at the top left corner of the cavity due to a drop in pressure which results in heat transfer from the wall to the gas, whereas viscous heat generation ($T > T_w$) results in heat transfer from the gas to the wall toward the right corner of the cavity. The direction of heat transfer is governed by both expansion cooling and viscous dissipation. The heat transfer plots in the driven cavity indicate that thermal energy transfer need not always be from a hot region to a cold region as continuum theory dictates. The temperature field and the heat flux streams predicted by the R26 equations are presented in Figure 15(b). In comparison with Figure 15(a), the R26 equations capture the temperature field and the heat flux streams quite well except that the R26 equations overpredict the temperature drop and rise in the top left and right corner of the cavity, respectively. On the other hand, the NSF equations cannot predict thermal field neither quantitatively nor qualitatively, as illustrated in Figure 15(c).
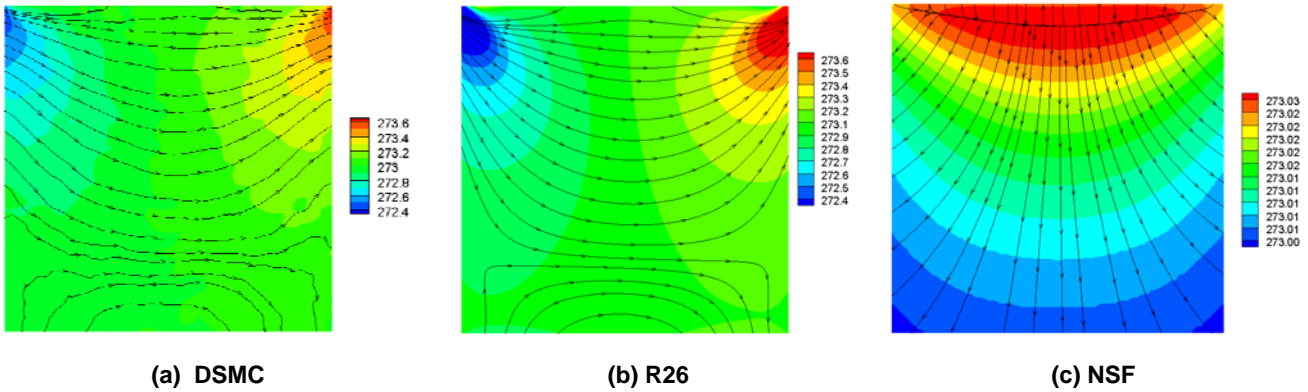
| (a) DSMC | (b) R26 | (c) NSF |

Figure 15: Comparison of heat flux stream traces overlaid on temperature contours computed
by (a) DSMC, (b) R26 and (c) NSF for the driven cavity at *Kn* = 0.2 and U$_w$ = 10 m/s.

The predicted profiles of velocity, *u* and *v*, shear stress, σ_{xy}, and temperature, *T*, by the R26 moment equations, along the vertical and horizontal lines across the cavity centre are plotted in Figures 16–18 in comparison with the DSMC data [55] of U$_w$ = 50 m/s and *Kn* = 0.1 and 0.5. When *Kn* = 0.1, the predicted velocities in both directions are in good agreement with the DSMC data as shown in Figure 16. As *Kn* increases to 0.5, the DSMC results show that the values of the slip velocity on the walls increase. However, the R26 equations overpredict about 10% of the slip velocity on the top moving wall. Away from the lid, the predicted *u* velocity agrees with the DSMC data quite well as shown in Figure 16(a). The agreement with the DSMC data for *v* velocity at *Kn* = 0.5 is not good close to the walls as well as away from the walls as plotted in Figure 16(b). However, the R26 equations predict the values of shear stress quite accurately on the vertical line for both Knudsen numbers as indicated in Figure 17(a). Figure 17(b) shows that the value of shear stress is overpredicted by the R26 equations on the horizontal line for *Kn* = 0.5. Here $\sigma_o = \mu U_w/L$ is a reference stress for normalization.
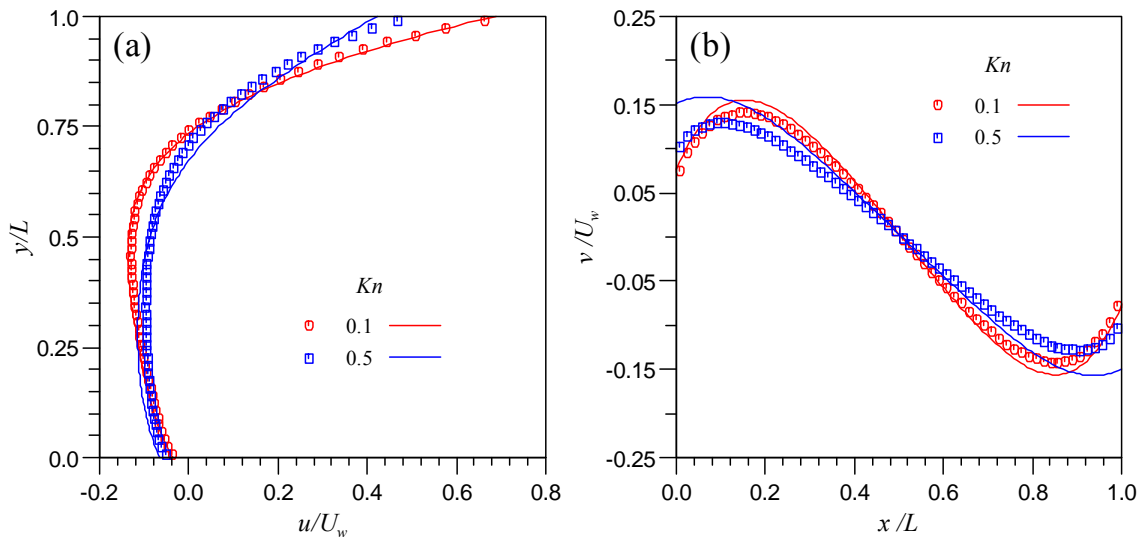

Figure 16: Comparison of normalised velocity profiles across the cavity centre.
Lid velocity U$_w$= 50 m/s. Symbols: DSMC [55]; Lines: the R26 equations.
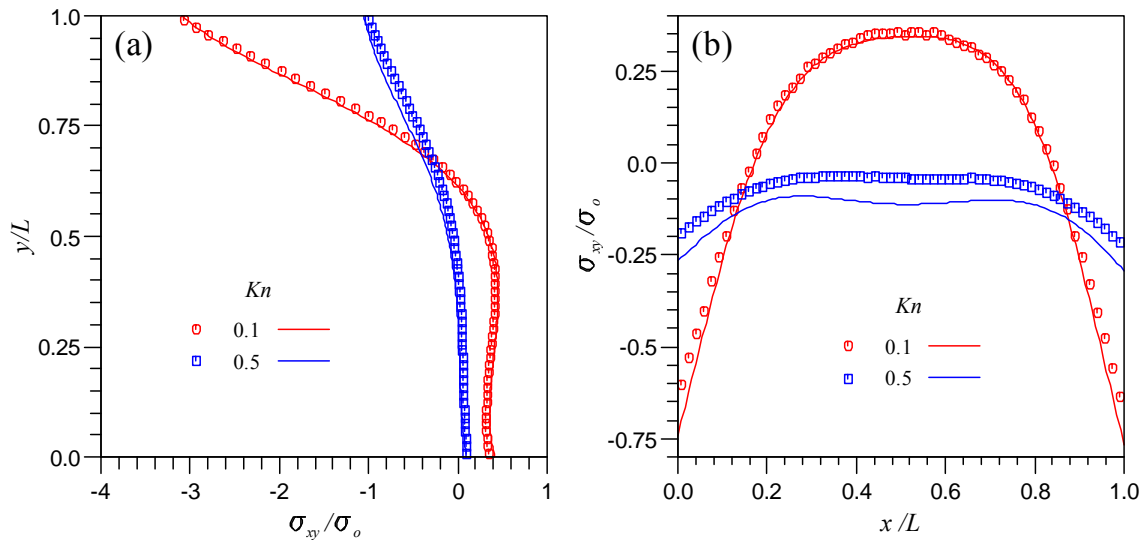**(a) u velocity on a vertical line; (b) v velocity on a horizontal line.**

**Figure 17: Comparison of normalised shear stress profiles across the cavity centre. Lid velocity
U_w= 50 m/s and $\sigma_o = \mu U_w/L$. Symbols: DSMC [55]; Lines: the R26 equations.
(a) Shear stress on a vertical line; (b) Shear stress on a horizontal line.**

The predicted temperature profiles on the vertical and horizontal lines across the cavity are plotted in
Figure 18 in comparison with the DSMC data, which are scattered. It is computationally expensive to
reduce statistical noise for temperature field with DSMC simulation, particularly for flows in MEMS.
Figure 18(a) shows that the gas temperature close to the moving lid is higher than the lid temperature. At
$Kn = 0.1$, the temperature of gas increases as it moves into the cavity, then drops after it enters into more
than 10% of the cavity depth. The R26 equations capture this trend well in good agreement with the
DSMC data. At $Kn = 0.5$, the maximum temperature of the gas on the vertical line across the cavity centre
is on the moving wall. The R26 equations underpredict the temperature jump significantly. The
temperature of the gas is lower than T_w on the left while higher than T_w on the right as shown in Figure
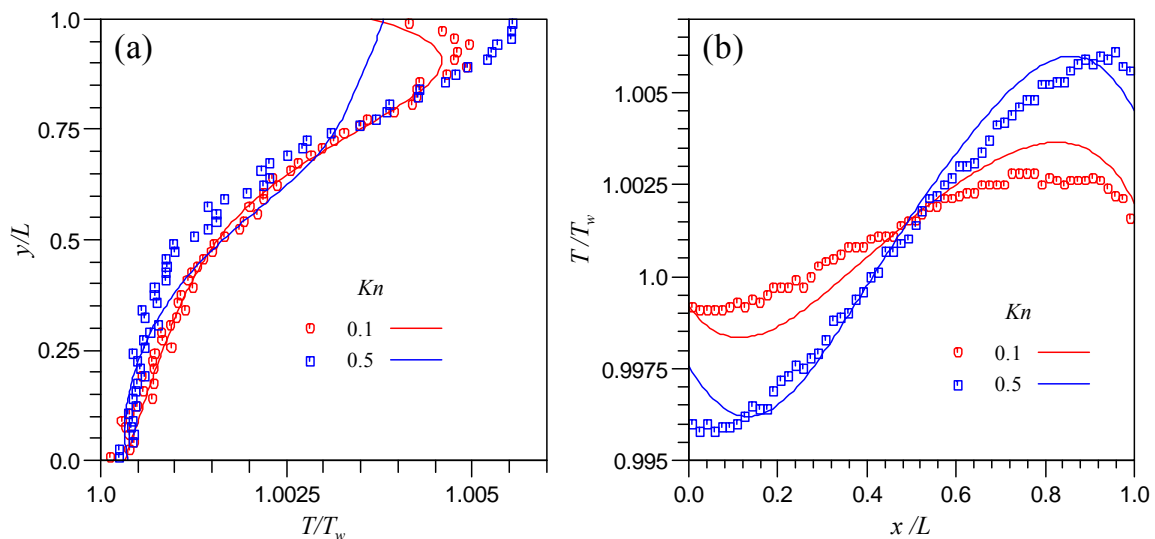18(b). The predictions of the R26 equations are in reasonable agreement with the DSMC data.

**Figure 18: Comparison of normalised temperature profiles across the cavity centre.
Lid velocity U_w= 50 m/s. Symbols: DSMC [55]; Lines: the R26 equations.
(a) temperature on a vertical line; (b) temperature on a horizontal line.**

7.5 Thermal Transpiration and Knudsen Pump

The phenomenon of thermal transpiration or creep was discovered by Reynolds in 1879, in which a gas will move along a solid surface due to inequalities of temperature [56]. It has been investigated theoretically and experimentally by various researchers over more than a century [57-65]. It is assumed that equal numbers of molecules arrive at the wall from the hot and cold regions. Molecules arriving from the hot region will have, on average, a higher velocity than those arriving from the cold region. Since the molecules are reflected diffusively at the wall, the resultant force on the wall due to the molecular collisions acts towards the cold region. An equal and opposite force is felt by the gas molecules, giving rise to a flow towards the hot region. Once the fluid starts to creep along the wall, the moving fluid layer interacts with the stagnant fluid layers adjacent to it, inducing a boundary layer. This phenomenon was used by Knudsen in 1910 to construct the first multistage thermal transpiration pump [58, 59].

A microscale gas pump is often required to form a complete micro system. Many issues have been encountered in attempting to shrink full-scale conventional pumps to microscales, such as manufacturing tolerances, pump oil, thermal inefficiency and short life time. The Knudsen pump has the advantages of no moving parts and supplementary pumping fluids. A typical multistage Knudsen pump is a long pipe or channel with a periodic structure consisting of alternately arranged narrow and wide dimensions. The temperature along the pipe or channel is also periodic with a distribution increasing in the narrow parts and decreasing in the wide parts. In the narrow parts where temperature increases, the pressure increases due to the non-equilibrium phenomenon of thermal creep. In the wide section, the thermal creep effect is less profound and the gas flow is closer to the continuum regime. One of the modern versions of the Knudsen pump was designed by Pham-Van-Diep et al. [66], the ith stage of which is illustrated in Figure 19. The performance of the modern Pham-Van-Diep pump has been studied by Vargo et al. [67] and Muntz et al. [68] using kinetic theory. Other modern Knudsen pumps are reported by McNamara and Gianchandani [69] and Pharas and McNamara [70].
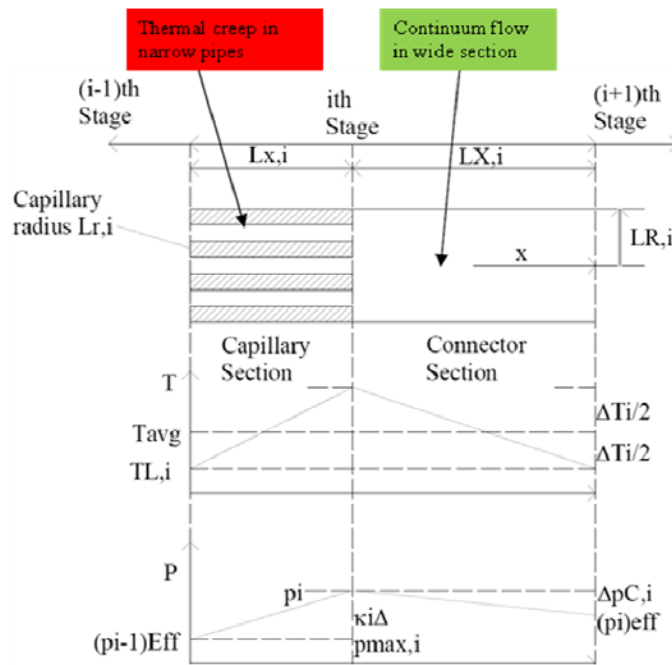

Figure 19: Illustrative ith stage of a Knudsen pump. Adapted from Ref. [67].

One of the major challenges in the design of the Knudsen pump is to ensure good thermal isolation between the hot and cold ends in the alternating heating and cooling structure. One way to avoid this

difficulty is to replace the alternating heating system by a central heating system. Illustrated in Figure 20 is a 3 staged Knudsen pump heated by a central heater on the right side to generate the necessary temperature gradient for thermal creep. The temperature gradient is largely determined by the thermal conductivity of the channel material and the length of the channels. As an example, it is assumed that temperature is linearly distributed between the hot and cold end with a temperature difference ΔT. The width of the narrow channel is designed to be 1 μm. The width of the wide channel is 5 times that of the narrow ones. The R26 equations are solved for different values of ΔT and Knudsen number Kn_o, which is based on the inlet condition.
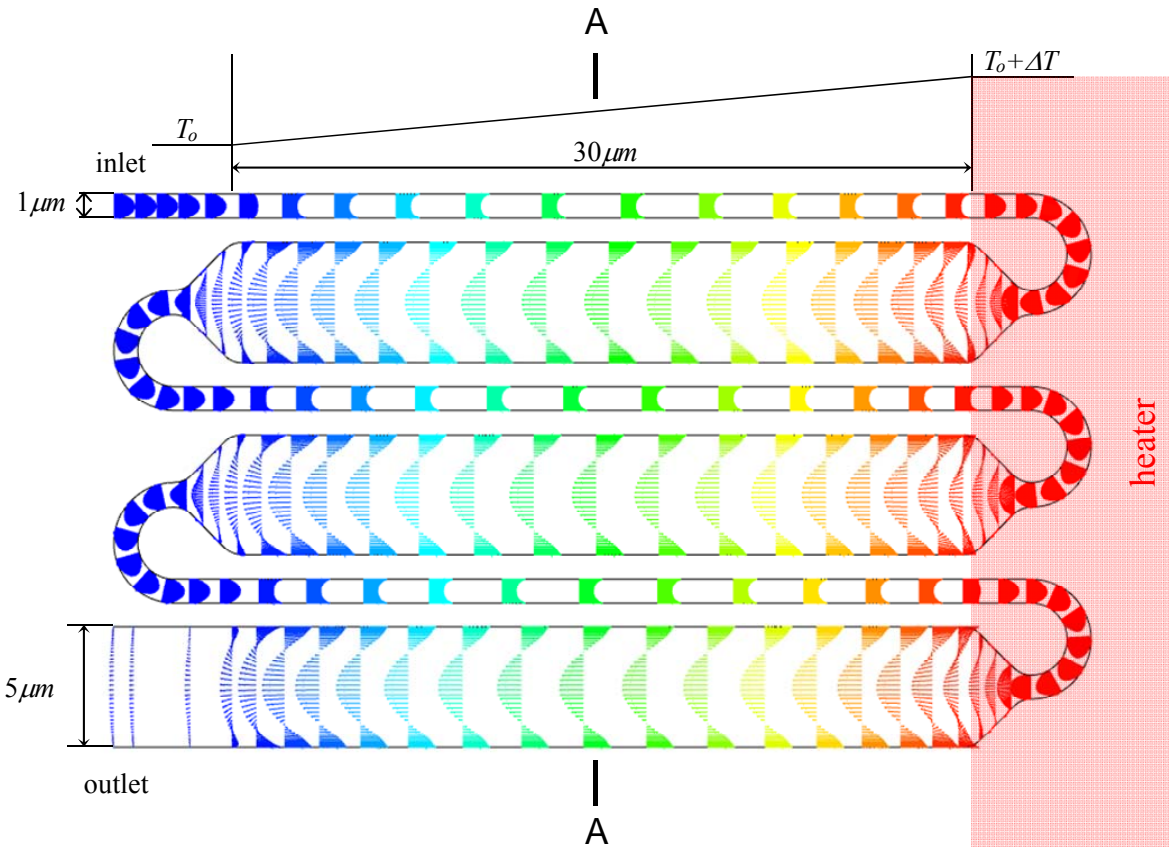

Figure 20: An illustration of a central 3 stage heated Knudsen pump and gas flow velocity vectors in the pump. Red colour indicates hot and blue cold. The temperature on the walls is linearly distributed.

Shown in Figure 20 are the velocity vectors in the central heated Knudsen pump for the case of $Kn_o = 0.1$ and $\Delta T = 2K$. Cold gas is driven towards the hot end in the narrow channels by thermal transpiration. In the wide channels, only the gas close to the walls is creeping towards the hot end. The gas away from the walls in the wide channels is pushed towards the cold end by the pressure generated in the narrow channels. The pressure changes Δp along the channel centre line from the inlet to the outlet are plotted in Figure 21 for $Kn_o = 0.1$ and $\Delta T = 1K$, $2K$ and $3K$, respectively. The pressure is built up in the narrow channels and drops in the wide channels and when the flow changes direction. The width ratio of the narrow and wide channels will affect the pressure distribution. When the temperature difference between the hot and cold end increases, the pressure difference between the inlet and outlet increases.
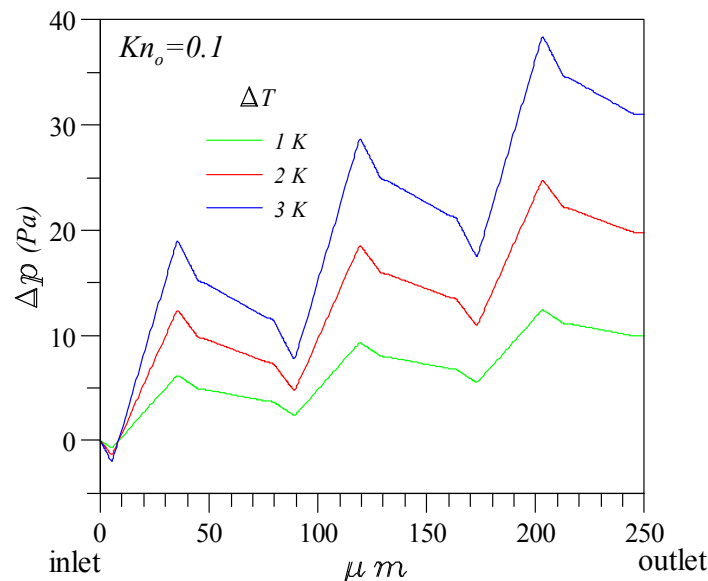
Figure 21: Pressure change from the inlet to the outlet along the channel centre line.

8.0   SUMMARY

Gas flows in micro-electro-mechanical-systems suffer from non-equilibrium effects. The conventional hydrodynamic model, the Navier-Stokes-Fourier equations, is unable to capture these effects correctly in the slip and early transition regimes. In this lecture, we demonstrate that hydrodynamic models can be extended to account for non-equilibrium effects by introducing high moment equations, which can be derived from kinetic theory, into hydrodynamic models. From Kramers' problem to the flow in a lid driven cavity, it is indicated that the R26 moment equation model, based on Grad's moment method and Struchtrup and Torrilhon's regularization procedure, can be used to predict non-equilibrium gas flows fairly accurately up to a Knudsen number of 0.5. The conventional numerical techniques for low speed flow in confined geometries can be readily used to solve the moment equations for engineering applications in MEMS.

9.0   REFERENCES

[1]   Karniadakis, G., Beskok, A. & Aluru, N., *Microflows and Nanoflows – Fundamentals and Simulation*, Springer, New York, 2005.

[2]   Beskok, A., "Validation of a New Velocity-Slip Model for Separated Gas Microflows," *Num. Heat Transfer*, Part B 40:451–471 (2001).

[3]   Cercignani, C., *Rarefied Gas Dynamics: From Basic Concepts to Actual Calculations*. Cambridge University Press, Cambridge, 2000.

[4]   Reese, J. M. & Zhang Y., "Simulating Fluid Flows in Micro and Nano Devices: The Challenge of Non-equilibrium Behaviour," *J. Comput. Theor. Nanosci.* 6:1–14 (2009).

[5]   Barber, R. W. & Emerson, D. R., "Challenges in Modeling Gas-Phase Flow in Microchannels: From Slip to Transition," Heat Transfer Eng. 27:3-12 (2006).

[6] Gad-el-Hak, M., "The Fluid Mechanics of Microdevices – The Freeman Scholar Lecture," *J. Fluids Eng*. 121, 5–33 (1999).

[7] Cercignani, C., *The Boltzmann Equation and Its Applications*. Springer-Verlag, New York, 1988.

[8] Ohwada, T., Sone, Y. & Aoki, K., "Numerical Analysis of the Poiseuille and Thermal Transpiration Flows Between Two Parallel Plates on the Basis of the Boltzmann Equation for Hard-Sphere Molecules," *Phys*. *Fluids* A 1:2042–2049 (1989).

[9] Mieussens, L., "Discrete-Velocity Models and Numerical Schemes for the Boltzmann-BGK Equation in Plane and Axisymmetric Geometries," *J. Comput*. *Phys*. 162:429–466 (2000).

[10] Bird, G., *Molecular Gas Dynamics and the Direct Simulation of Gas Flows*, Claredon Press, Oxford, 1994.

[11] Chapman, S. & Cowling, T. G., *The Mathematical Theory of Non-uniform Gases*, Cambridge University Press, Cambridge, 1970.

[12] Grad, H., "On the Kinetic Theory of Rarefied Gases," *Commun*. *Pure Appl*. *Math*. 2:331–407 (1949).

[13] Struchtrup, H. & Torrilhon, M., "Regularization of Grad's 13 Moment Equations: Derivation and Linear analysis," *Phys*. *Fluids* 15:2668–2680 (2003).

[14] Gu, X. J. & Emerson, D. R., "A High-order Moment Approach for Capturing Non-equilibrium Phenomena in the Transition Regime," *J. Fluid Mech*. 636:177–216 (2009).

[15] Gu, X. J. & Emerson, D. R., "A Computational Strategy for the Regularised 13 Moment Equations with Enhanced Wall-boundary Conditions," *J. Comput*. *Phys*. 225:263–283 (2007).

[16] Torrilhon, M. & Struchtrup, H., "Boundary Conditions for Regularised 13-Moment-Equations for Micro-Channel-Flows," *J*. *Comput*. *Phys*. 227:1982–2011 (2008).

[17] Struchtrup, H. & Torrilhon, M., "Higher-Order Effects in Rarefied Channel Flows," *Phys. Rev. E* 78, 046301 (2008).

[18] Taheri, P. Torrilhon, M. & Struchtrup, H., "Couette and Poiseuille Microflows: Analytical Solutions for Regularised 13-Moment Equations," *Phys*. *Fluids* 21, 017102 (2009).

[19] Gu. X. J., Emerson. D. R. & Tang. G. H., "Kramers' Problem and the Knudsen Minimum: A Theoretical Analysis Using a Linearised 26-Moment Approach," Contin. Mech. Thermodyn. 21:345–36 (2009).

[20] Taheri, P. & Struchtrup, H., "An Extended Macroscopic Transport Model for Rarefied Gas Flows in Long Capillaries with Circular Cross Section," *Phys. Fluids* 22, 112004 (2010).

[21] Gu, X. J., Emerson, D. R. & Tang, G. H., "Analysis of the Slip Coefficient and Defect Velocity in the Knudsen Layer of a Rarefied Gas Using the Linearised Moment Equations," *Phys. Rev. E* 81, 016313, (2010)

[22] Ferziger, J. H. & Perić, M., *Computational Methods for Fluid Dynamics*, 2nd Ed, Springer-Verlag Berlin-Heidelberg, 1999.

[23] Toro, E. F., *Riemann Solvers and Numerical Methods for Fluids Dynamics: A Practical Introduction*, 2nd ed., Springer, Berlin, 1999.

[24] Harten, A., "High-Resolution Schemes for Hyperbolic Conservation-Laws," *J. Comput. Phys.* 49:357–393 (1983).

[25] Liu, X. D. & Osher, S., "Convex ENO High Order Multi-Dimensional Schemes without Field by Field Decomposition or Staggered Grids," *J. Comput. Phys.* 142:304–330 (1998).

[26] Gu, X. J., John, B., Tang, G. H. & Emerson, D. R., in preparation for *Computer and Fluids* (2011).

[27] Struchtrup, H., *Macroscopic Transport Equations for Rarefied Gas Flows*. Springer-Verlag, Berlin Heidelberg, 2005.

[28] Gorban, A. N., Karlin, I. V. & Zinovyev, A. Y., "Constructive Methods of Invariant Manifolds for Kinetic Problems," *Phys. Rep.* 396:197–403 (2004).

[29] Struchtrup, H., "Linear Kinetic Transfer: Moment Equations, Boundary Conditions, and Knudsen Layer," *Physica A* 387:1750–1766 (2008).

[30] Truesdell, C. & Muncaster, R. G., *Fundamentals of Maxwell's Kinetic Theory of a Simple Monotomic Gas*, Academic Press, New York, 1980.

[31] Maxwell, J. C., "On Stresses in Rarified Gases Arising from Inequalities of Temperature", *Phil. Trans. Roy. Soc. (Lond.)* 170:231–256 (1879).

[32] Leonard, B. P., "A Stable and Accurate Convection Modelling Procedure Based on Quadratic Upstream Interpolation," *Comput. Mech. Appl. Mech. Engrg.* 19, 59–98 (1979).

[33] Gaskell, P. H. & Lau, A. K. C., "Curvature-Compensated Convective-Transport - SMART, A New Boundedness-Preserving Transport Algorithm," *Int. J. Numer. Meth. Fluids* 8, 617–641 (1988).

[34] Alves, M. A., Oliveira, P. J. & Pinho, F. T., "A Convergent and Universally Bounded Interpolation Scheme for the Treatment of Advection," *Int. J. Numer. Meth. Fluids* 41, 47–75 (2003).

[35] Patankar, S. V., *Numerical Heat Transfer and Fluid Flow*. McGraw-Hill, New York, 1980.

[36] Issa, R.I., "Solution of the Implicitly Discretised Fluid Flow Equation by Operator-Splitting," *J. Comput. Phys.* 62:40–65 (1985).

[37] Struchtrup, H. & Torrilhon, M., "H Theorem, Regularization and Boundary Conditions for Linearised 13 Moment Equations," *Phys. Rev. Lett.* 99, 014502 (2007).

[38] Kramers, H. A., "On the Behaviour of a Gas near a Wall," *Suppl. Nuovo Cimento* 6:297–304 (1949).

[39] Albertoni, S., Cercignani, C. & Gotusso, L., "Numerical Evaluation of the Slip Coefficients," *Phys. Fluids* 6:993–996 (1963).

[40] Loyalka, S. K. "Velocity Defect in the Knudsen Layer of Kramer's Problem," *Phys. Fluids* 18:1666–1669 (1975).

[41] Loyalka, S. K. & Hickey, K. A., "Velocity Slip and Defect: Rigid Sphere Gas," *Phys. Fluids* A 1: 612–614 (1989).

[42] Loyalka, S. K. & Tompson, R. V., "The Velocity Slip Problem: Accurate Solutions of the BGK Model Integral Equation," *Euro. J. Mech. B/Fluids* 28:211–213 (2009).

[43] Siewert, C. E., "Kramers' Problem for a Variable Collision Frequency Model," *Euro. J. Appl. Math.* 12:179–191 (2001).

[44] Cercignani, C., Lampis, M. & Lorenzani, S., "Variational Approach to Gas Flows in Microchannels," *Phys. Fluids* 16:3426–3437 (2004).

[45] Sharipov, F. & Kalempa, D., "Gas Flow near a Plate Oscillating Longitudinally with an Arbitrary Frequency," *Phys. Fluids* 19, 017110 (2007).

[46] Sharipov, F. & Kalempa, D., "Oscillatory Couette flow at arbitrary frequency over the whole range of the Knudsen number," *Microfluid Nanofluid* 4:363-374 (2008).

[47] Gu, X. J. & Emerson, D. R., "Modeling oscillatory flows in the transition regime with a high-order moment method," *Microfluid Nanofluid* DOI 10.1007/s10404-010-0677-1 (2011).

[48] Park, J. K., Bahukudumbi, P. & Beskok, A., "Rarefaction Effects on Shear Driven Oscillatory Gas Flows: A Direct Simulation Monte Carlo Study in the Entire Knudsen Regime," *Phys. Fluids* 16:317–330 (2004).

[49] Hadjiconstantinou, N. G., "Oscillatory Shear-driven Gas Flows in the Transition and Free-Molecular-Flow Regimes," *Phys. Fluids* 17:100611 (2005).

[50] Emerson, D. R., Gu, X. J., Stefanov, S. K., Yuhong, S. & Barber, R. W., "Nonplanar Oscillatory Shear Flow: From the Continuum to the Free – Molecular Regime," *Phys Fluids* 19, 107105 (2007).

[51] Shankar, P. N. & Deshpande, M. D., "Fluid Mechanics in the Driven Cavity," *Annu. Rev. Fluid Mech.* 32:93–136 (2000).

[52] Naris, S. & Valougeorgisa, D., "The Driven Cavity Flow over the Whole Range of the Knudsen Number," *Phys. Fluids* 17, 097106 (2005).

[53] Tang, G. H., Tao, W. Q. & He, Y. L., "Lattice Boltzmann Method for Gaseous Microflows Using Kinetic Theory Boundary Conditions," *Phys. Fluids* 17, 058101 (2005).

[54] Mizzi, S., Emerson, D. R., Stefanov, S. K., Barber, R. W. & Reese, J. M., "Effects of Rarefaction on Cavity Flow in the Slip Regime," *J. Comput. Theor. Nanosci.* 4:817– 822 (2007).

[55] John, B., Gu, X. J. & Emerson, D. R., "Investigation of Heat and Mass Transfer in a Lid-Driven Cavity Under Nonequilibrium Flow Conditions," *Num. Heat Transfer*, Part B 58: 287– 303 (2010).

[56] Reynolds, O., "On Certain Dimensional Properties of Matter in the Gaseous State," *Phil. Trans. Royal Soc. Lond.* 170:727 – 845 (1879).

[57] Graham, T., "On the Molecular Mobility of Gases," *Phil. Trans Royal Soc. Lond.* 153:385-405 (1863).

[58] Knudsen, M., "Eine Revision der Gleichgewichsbedingung der Gase, Thermische Molekularströmung," *Annalen der Physik*, 336: 205–229 (1909).

[59] Knudsen, M., "Thermischer Molekulardruck der Gase in Röhren," *Annalen der Physik*, 338:1435–1448 (1910).

[60] Liang, S. C., "On the Calculation of Thermal Transpiration," *Canadian J. of Chem*. 33:279-285 (1955).

[61] Cercignani, C. & Daneri, A., "Flow of Rarefied Gas between Two Parallel Plates," *J. Appl. Phys*. 34:3509-3513 (1963).

[62] Sone, Y., "Thermal Creep in Rarefied Gas," *J. Phys. Soc. Jpn*. 21:1836-1837 (1966).

[63] Loyalka, S. K., "Thermal Transpiration in a Cylindrical Tube," *Phys. Fluids* 12:2301-2305 (1969).

[64] Sone, Y., "Flows induced by Temperature Fields in a Rarefied Gas and Their Ghost Effect on the Behavior of a Gas in the Continuum Limit," Annu. Rev. Fluid Mech. 32:779-811 (2000).

[65] Han, Y.-L., Muntz, P. E., Alexeenko, A. & Young, M., "Experimental and Computational Studies of Temperature Gradient–Driven Molecular Transport in Gas Flows Through Nano/Microscale Channels," *Nano. Micro. Thermophys. Eng*. 11:151–175 (2007).

[66] Pham-Van-Diep, G., Keeley, P., Muntz, E. P. & Weaver, D. P., "A Micromechanical Knudsen Compressor," in J. Harvey and G. Lord (eds.), *Rarefied Gas Dynamics*, pp. 715–721, Oxford University Press, Oxford, 1995.

[67] Vargo, S. E., Muntz, E.P., Shiflett, G.R. & Tang, W.C., "The Knudsen Compressor as a Micro and Macro Scale Vacuum Pump without Moving Parts or Fluids," *J. Vac. Sci. and Tech*. A 17:2308–2313 (1999).

[68] Muntz, E. P., Sone, Y., Aoki, K., Vargo, S. & Young, M., "Performance Analysis and Optimization Considerations for a Knudsen Compressor in Transitional Flow," *J. Vac. Sci. and Tech*. A, 20:214-224 (2002).

[69] McNamara, S. & Gianchandani, Y. B., "On-Chip Vacuum Generated by a Micromachined Knudsen Pump," *J. Micrelectroeng. Syst*. 14:741:746 (2005).

[70] Pharas, K. & McNamara, S., "Knudsen Pump Driven by a Thermoelectric Material," *J. Micromech. Microeng*. 20:125032 (2010).